Seismic Reflection Study of a Shallow Aquifer During a Pumping Test

by

Bradley A. Birkelo

B.S. Geology, University of Minnesota, 1982

B.S. Geophysics, University of Minnesota, 1983

Submitted to the Department
of Geology and the Faculty of the
Graduate School of the University
of Kansas in partial fulfillment
of the requirements for the degree
of Master of Science.

Chairman

Committee Members

For the Department

July 13, 1987
Date Thesis Accepted

Abstract

This study develops a seismic-reflection method that gives detailed hydrologic and geologic information about a shallow aquifer without the need for many observation wells. Seismic-reflection surveys were used to follow the drawdown in a shallow aquifer during a pumping test. Using severe analog low-cut filters and 1/4-m geophone spacings, 335-Hz reflections were obtained from the top of the saturated zone 2.7 m deep. The reflections moved down in time as the saturated zone dropped in response to pumping. The dominant frequency and bandwidth both dropped during pumping, indicating a more diffuse reflecting boundary. Slight elevation rises in the reflector of as much as 0.3 m at specific locations on the CDP sections may indicate a higher elevation of the capillary fringe and therefore finer sediments in those locations. The top of the saturated zone dropped less than expected and did not show signs of the cone of depression. This, combined with drawdown data and gamma-ray logs, led to the conclusion that an intermediate clay layer, previously thought to be discontinuous, caused a perched water table in the vicinity of the pumping well.

Analysis of the stacking velocities and correlation coefficients showed that water retained in the soil layer is probably responsible for most of the lateral variation of the stacking velocities. Amplitude-versus-offset analysis of the common-offset data show there are two offsets where the multiple reflection reaches maximum amplitude, possibly where the seismic energy is incident on the reflecting interface at the P- and S-wave critical angles.

Dedication

This thesis is dedicated to the memory of my father, Donald J. Birkelo.

Acknowledgments

There were many people who helped me during my tenure at the University of Kansas. I'd like to thank my advisor, Don Steeples, who provided me with an idea to work on, the freedom to approach it as I saw fit, and some needed advice and direction along the way. The working environment in Don's seismic lab was second to none and the pheasants on his farm were more clever than I. I also thank my other committee members, Don Sprowl and Paul Enos, who gave helpful and timely suggestions. Rick Miller deserves special thanks for teaching me most of what I know about practical reflection seismology. His insights and ideas were instrumental in the success of this project, especially early on. Jeff Treadway, Paul Myers, and Rick Miller made numerous long, one-day trips to Great Bend to help collect the data, occasionally battling hail, lightning, bitter cold, and persistent insects. Marios Sophocleous set up the near-perfect site for these experiments and allowed me access to his pumping-test data. Pat Acker did an outstanding producing some of the figures and I'm sure she was quite happy once it was too late to change anything else. Marla Adkins-Heljeson offered editorial suggestions and formally introduced me to the hyphen. Her Macintosh computer produced most of the figures in this thesis. I'd also like to thank Dale Weller for allowing me access to his farm several times. Most of all, I'd like to thank my parents for the years of moral and financial support and for teaching me the value of learning.

Table of Contents

	Page
Abstract	ii
Dedication	iii
Acknowledgments	iv
Table of Contents	v
List of Figures	vi
List of Tables	vii
Introduction	1
Previous Studies	2
Geologic Setting	3
Preliminary Testing	9
Analysis of Field Data	20
Results	28
Shallow reflection	28
Additional processing	43
Reflection topography	51
Stacking velocities and correlation coefficients	53
Conclusions	59
Appendix	61
Amplitude versus offset	61
Direct/refracted wave	67
Interference effects	67
Multiple reflection	69
References	72

List of Figures

Figure 1- Location of pumping-test site.

Figure 2- Map of pumping-test site.

Figure 3- Geologic cross section.

Figure 4- Drillers' and gamma logs.

Figure 5- Geologic cross section at pumping-test site.

Figure 6- Prepumping water levels.

Figure 7- Maximum-drawdown water levels.

Figure 8- January 23rd field record- 1-m geophone spacing.

Figure 9- January 23rd field record- 1/4-m geophone spacing.

Figure 10- Amplitude spectrum showing filtering effects.

Figure 11- Geophone damping comparison.

Figure 12- Split-spread and end-on geometries.

Figure 13- Walkaway test.

Figure 14- Pumping-test field records.

Figure 15- Amplitude spectrum identifying major energy peaks.

Figure 16- Amplitude spectrum of the reflected wavelet.

Figure 17- CDP processing steps.

Figure 18- April 17th CDP section.

Figure 19- April 24th CDP section.

Figure 20- April 28th CDP section.

Figure 21- April 19th, 24th, and 28th moisture profiles.

Figure 22- April 29th CDP section and moisture profile.

Figure 23- August 14th CDP section and moisture profile.

Figure 24- Elevation graphs of the top of the saturated zone.

Figure 25- Flow patterns at pumping-test site.

List of Figures (continued)

Figure 26- Processing diagram with additional processing steps.

Figure 27- Explanation of additional processing steps.

Figure 28- April 17th CDP section with additional processing.

Figure 29- April 24th CDP section with additional processing.

Figure 30- April 28th CDP section with additional processing.

Figure 31- April 29th CDP section with additional processing.

Figure 32- August 14th CDP section with additional processing.

Figure 33- True-relative-amplitude CDP sections.

Figure 34- April 17th field record with weak reflection.

Figure 35- Calculated stacking velocities.

Figure 36- Calculated correlation coefficients.

Figure 37- Common-offset geometry.

Figure 38- April 17th common-offset gathers.

Figure 39- April 24th common-offset gathers.

Figure 40- April 28th common-offset gathers.

Figure 41- April 29th common-offset gathers.

Figure 42- April 17th common-offset gathers with seismograph gains removed.

List of Tables

Table 1 - Recording parameters.

Introduction

The role of seismic methods in ground-water investigations has traditionally been to supply information on the subsurface geology of an area of interest. Typically, refraction surveys have been employed to determine the thickness of unconsolidated sediments over bedrock although they can be used to roughly determine the depth to the water table (Eaton, 1974). Most ground-water data are obtained though direct measurements in observation wells, limiting information to a series of widely spaced points with aquifer properties inferred between and beyond the wells. If closely spaced data are necessary, many wells are needed, often at a high cost. In some areas, such as hazardous-waste sites, it may not be possible or desirable to obtain hydrologic data by such traditional means. This study shows that shallow seismic-reflection surveys possess the potential to provide direct hydrologic information at a point without direct well measurements.

Seismic-reflection methods have not been commonly used for ground-water investigations in the past for several reasons. It can be difficult to record and identify reflections from shallow interfaces because their amplitudes tend to be smaller than the ground roll which is also present (Steeples and Knapp, 1982). Until the recent advent of seismic processing on microcomputers, the processing costs were about double the cost of collecting the data. In addition, many problems such as spatial aliasing and the air-coupled wave can cause erroneous interpretations (Steeples and Miller, 1986).

Previous Studies

Much of the emphasis in geophysical research at the Kansas Geological Survey (KGS) has been in the area of high-resolution, shallow seismic reflection. The current ideas and practices at the KGS concerning the collection of shallow seismic-reflection data are presented in two papers by Knapp and Steeples (1986a,b). Present methods rely heavily on the optimum-window technique (Hunter et al., 1984) to obtain reflections without the interference from nonreflected energy and on the common-depth-point stacking method (CDP) originally developed by Mayne (1962).

In spite of the many applications of high-resolution seismic reflection, there are no examples in the literature where the water table was specifically the target of a reflection survey. Schepers (1975) reported obtaining a reflection from the ground-water surface in a paper that described a technique for resolving thin near-surface layers. Steeples and Knapp (1982) mention recording a water-table reflection while testing seismic sources. In a typical unconfined aquifer, both density and seismic P-wave velocity are greater below the water table than for the unsaturated sediments above, making the water table theoretically an excellent reflector of seismic energy. With this in mind, an experiment was conducted during an aquifer-pumping test to attempt to follow the water table seismically as it was drawn down.

Geologic Setting

The site chosen for this experiment was about 60 m southwest of the Arkansas River, 6 km east of Great Bend, Kansas (Figure 1). The KGS conducted an eight-day pumping test to study the interaction of the shallow alluvial aquifer with the Arkansas River. The pumping test was excellent for our seismic experiments because the test was long enough to allow some degree of stabilization of the water table at the pumping level. Also, the 1750 gpm of water pumped from the 20-inch-diameter well stressed the aquifer sufficiently to draw down the water table and create a large cone of depression. The 25 observation wells on the test site provided excellent hydrologic and geologic control (Figure 2).

The Pleistocene and Recent alluvium that make up the aquifer of interest consist of fine-to-coarse sand, gravel, and silt as shown in the generalized cross section adapted from Latta (1950) (Figure 3). Drillers' logs from the observation wells show mostly coarse feldspathic sand and gravel with discontinuous, thin clay layers (Figure 4). The depth to the alluvium-bedrock interface was 29 m at the pumping well and this correlated well with calculations from the preliminary seismic data.

The generalized site stratigraphy shows two prominent clay layers, the lower being thicker and more continuous over the test site (Figure 5). At the time of the test, the continuous extent of the lower clay wasn't realized. It was assumed that the clay layer was discontinuous and that the aquifer functioned as one unit from bedrock to surface, an incorrect assumption as shown later.

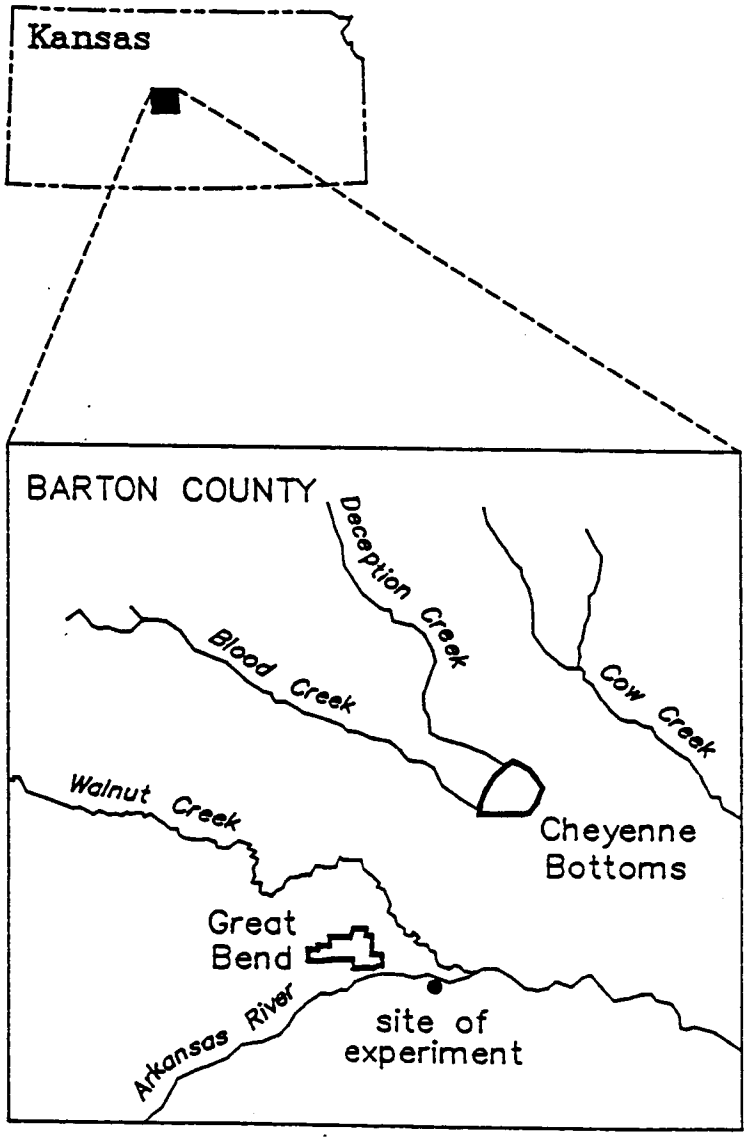

Figure 1 - Location of the pumping-test site.

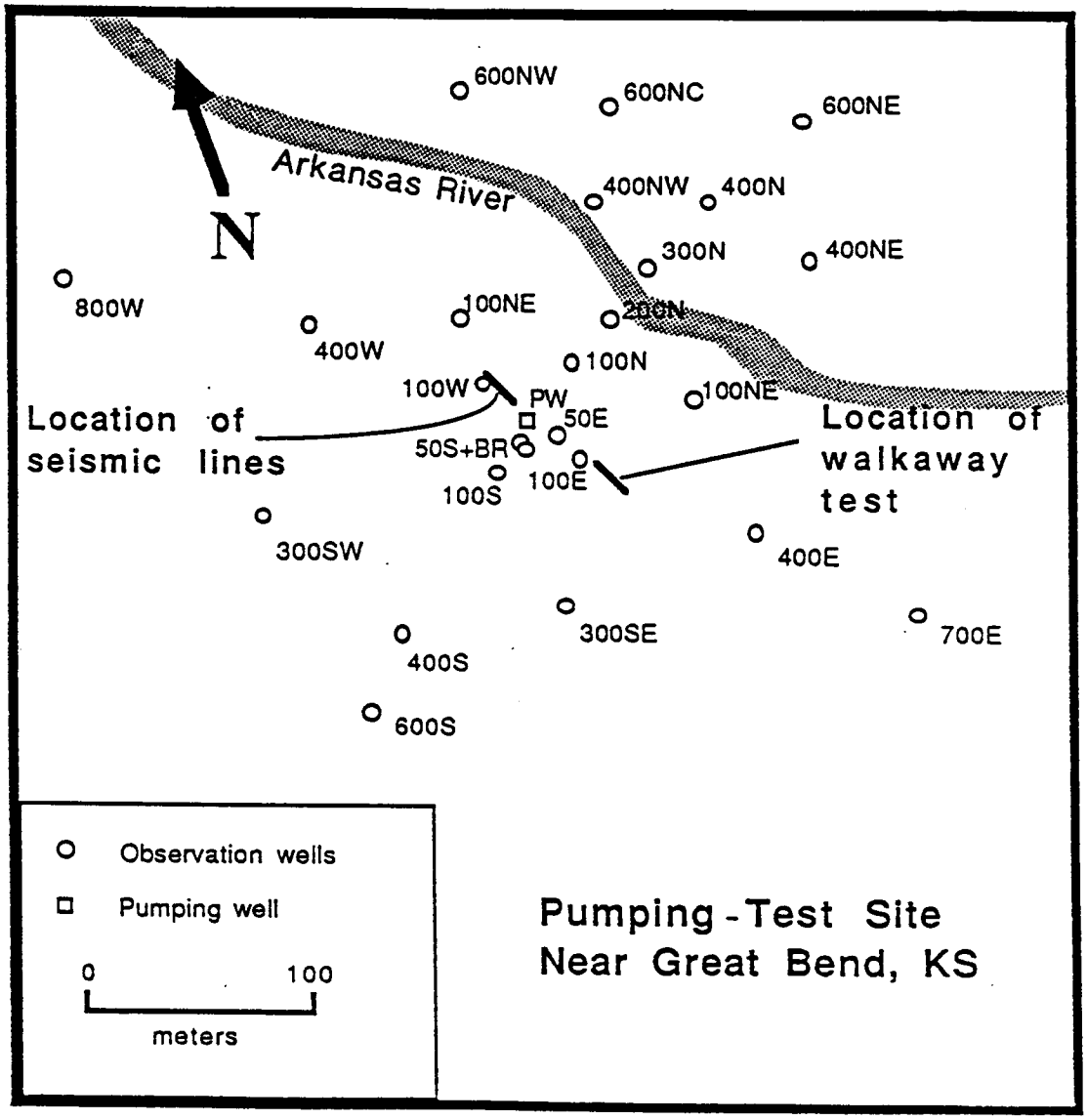

Figure 2 - Site map showing the location of the pumping well (PW), 25 observation wells, the walkaway test, and the seismic lines. The large number of wells provide excellent hydrologic and geologic control.

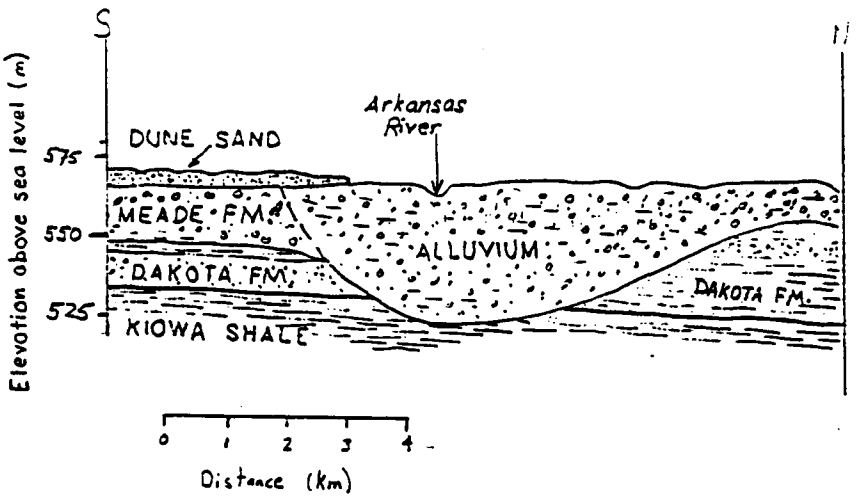

Alluvium - Recent and Pleistocene - Very coarse gravel, sand, and silt comprising stream deposits in the larger valleys.

Dune Sand - Recent and Pleistocene - Fine- to medium-grained wind-blown sand containing minor amounts of silt, clay, and coarse sand.

Meade Formation - Pleistocene - Interbedded lenses of unconsolidated gravel, sand, and silt. Caliche is common throughout the formation.

Dakota Formation - Cretaceous - Alternating beds or lenses of varicolored clay, shale, siltstone, and fine- to coarse-grained sandstone. Contains "ironstone" in thin beds, lignite, and a little pyrite.

Kiowa Shale - Cretaceous - Light-gray to black shale and sandy shale, containing beds or lenses of fine- to medium-grained sandstone and thin beds of hard calcareous sandstone and sandy limestone. Pyrite, gypsum, shell fragments, and cone-in-cone calcite are common.

Figure 3 - Diagrammatic geologic cross section adapted from Latta (1950). The cross section runs north-south through the eastern edge of Great Bend.

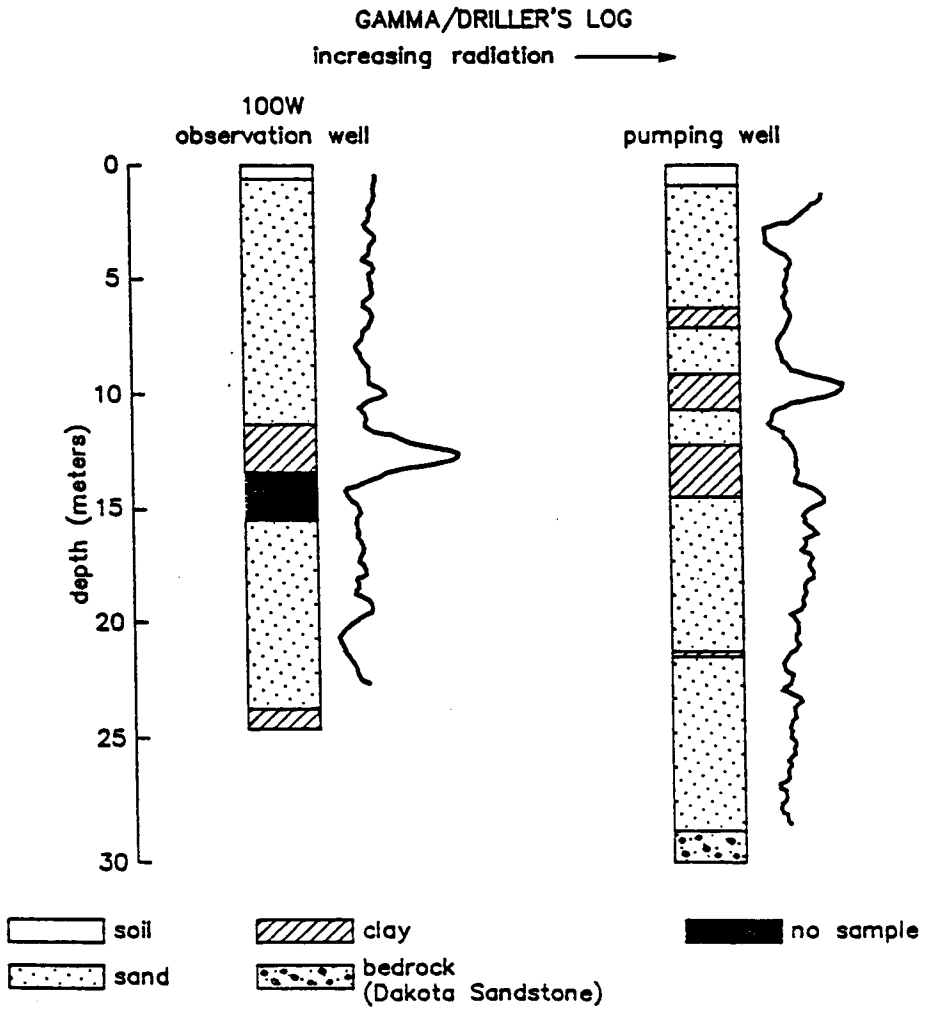

Figure 4 - Drillers' and gamma-ray logs from wells near the seismic lines (see Figure 2).

Figure 5 - Diagrammatic cross section though the pumping-test site based on drillers' and gamma-ray logs. The continuous nature of the clay layer at 10-13 m depth was not recognized until after the analysis of the seismic and hydrologic data. Note that all of the wells were screened below the clay layer.

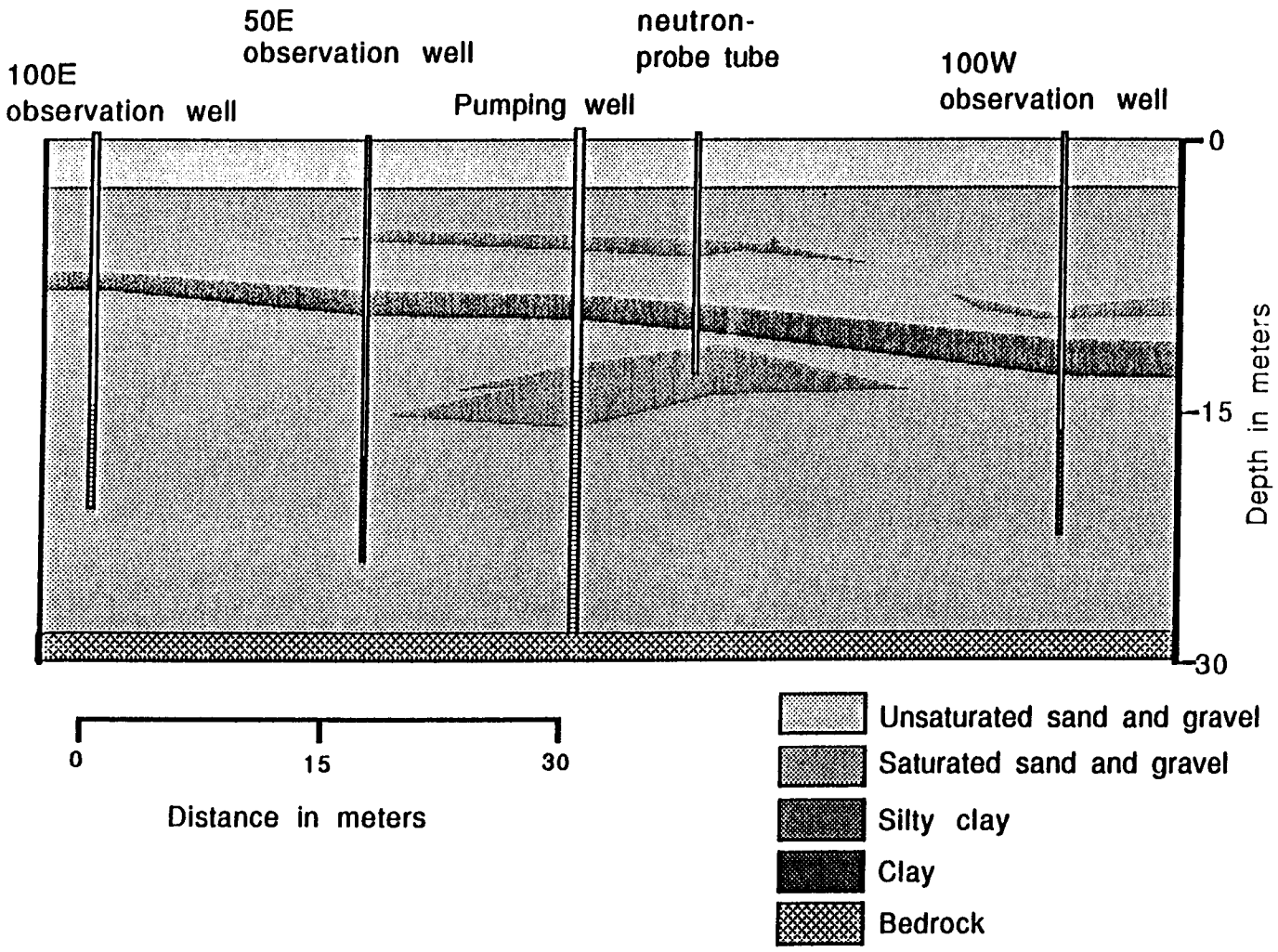
100E
observation well
50E
observation well
Pumping well
neutron-
probe tube
100W
observation well
0
15
30
Depth in meters
0
15
30
Distance in meters
Unsaturated sand and gravel
Saturated sand and gravel
Silty clay
Clay
Bedrock

The prepumping water levels at the test site show the pumping well is close to the center of a local water-table high, perhaps due to a greater elevation of the clay layer (Figure 6). Water levels at maximum drawdown show a well-developed cone of depression (Figure 7). The asymmetric cone of depression indicates recharge from the northeast. The seismic lines were shot over a portion of the cone of depression that had 2.5-5.0 m of drawdown. It is important to keep this in mind when interpreting the seismic sections collected during the pumping test.

Preliminary Testing

The key to the success in recording very shallow seismic reflections at this site was the proper choice of equipment and recording parameters. Of the seven seismic lines shot at the Great Bend pumping-test site, the first two lines were for the purpose of testing new analog filters and geophone dampers and to set up the recording parameters for the CDP lines to be shot during the pumping test. These two days of preliminary testing were important in choosing parameters best suited to these experiments.

The seismograph used in these experiments, an Input/Output DHR 2400, is a 24-channel system with 12-bit (11-bit plus sign) analog-to-digital (A/D) conversion and a wide selection of pre-A/D analog filters. The DHR 2400 is a fixed-gain system that is capable of sampling at time intervals of as short as 1/4 millisecond. IA-6 amplifiers that had 120-nanovolts rms peak-to-peak background noise were used to help improve the signal-to-noise ratio.

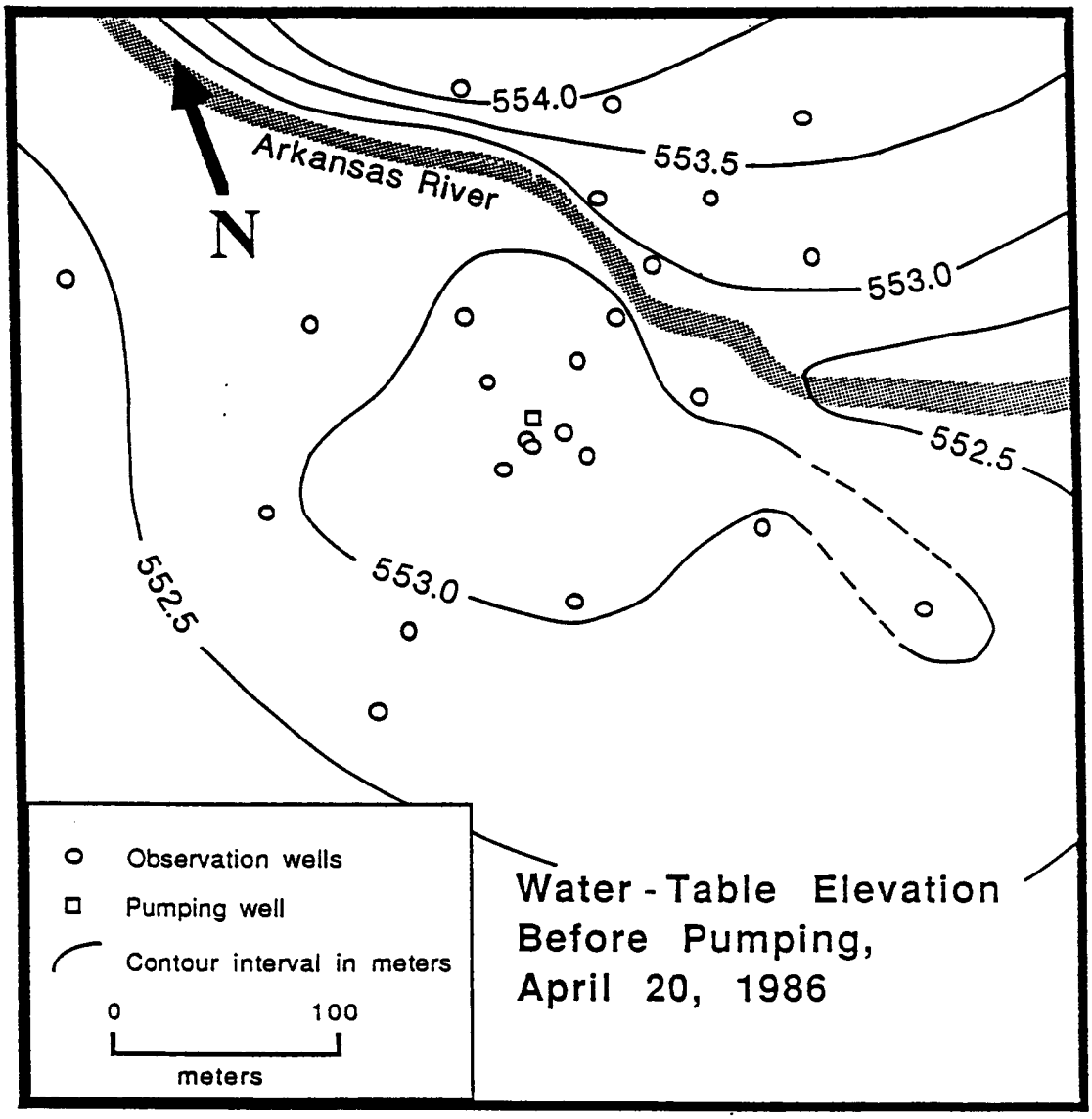

Figure 6 - Water-table-elevation map of the pumping-test site before pumping. The higher water table elevation around the pumping well may be because the continuous clay layer has a higher elevation in the vicinity of the pumping well causing a perched water table in the area.

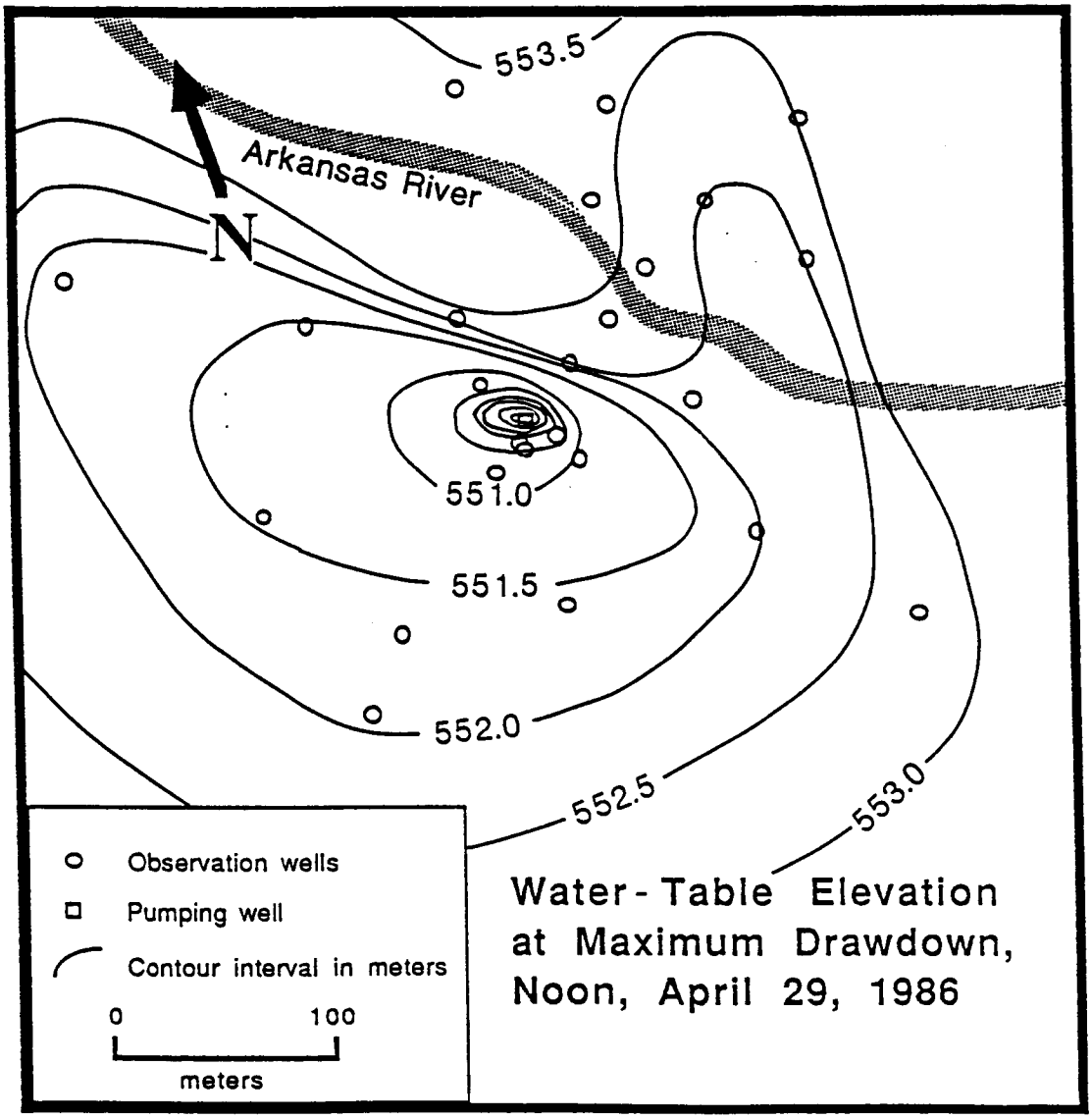

Figure 7 - Water-table elevation map at maximum drawdown showing the cone of depression as measured from the observation wells. The asymmetric cone of depression indicates recharge from the northeast. The extension of the cone to the north of the river indicates that the river does not act as a no-flow boundary. Drawdown under the seismic lines ranged from 2.5 m to 5 m. The elevation at the pumping well was 545.15 m.

The seismic source was a single 180-grain bullet fired vertically into the ground from a 30.06 hunting rifle. This rifle was modified by adding an air-blast-containment device that silenced much of the sound of the shot, thereby reducing the air-coupled wave on the seismic records. A motion sensor was mounted on the gun and when the gun fired, the movement sent a signal to trigger the seismograph to start recording. This source has been effective for some of the very shallow work done by the KGS (Treadway, 1987; Branham, 1986) and is capable of producing frequencies of several hundred hertz (Miller et al., 1986).

The receivers were single Mark Products 100-Hz geophones that have a 6-dB/octave rolloff below 100 Hz. This means that at 50 Hz the response is down 6 dB and at 25 Hz the response is down 12 dB, etc. They provided low-cut filtering in addition to that from the analog filters in the seismograph.

The first day of testing at the pumping-test site was in January 1986. The main goal of that day's testing was to obtain a reflection from the water table. The first reflection record shot on the first day of testing used a geophone spacing of 1 m, a source-to-closest-receiver offset of about 1 m, and a pre-A/D low-cut filter of 480 Hz (Figure 8). Geophones were undamped for this experiment. While reflections are visible from 32 msec to about 57 msec, the shallowest of these was from a depth calculated to be about 20 m. The water table was expected to be around 2-7 m below ground surface so the geophones were moved to a spacing of 1/4 m to better view the close offsets where shallower reflections,

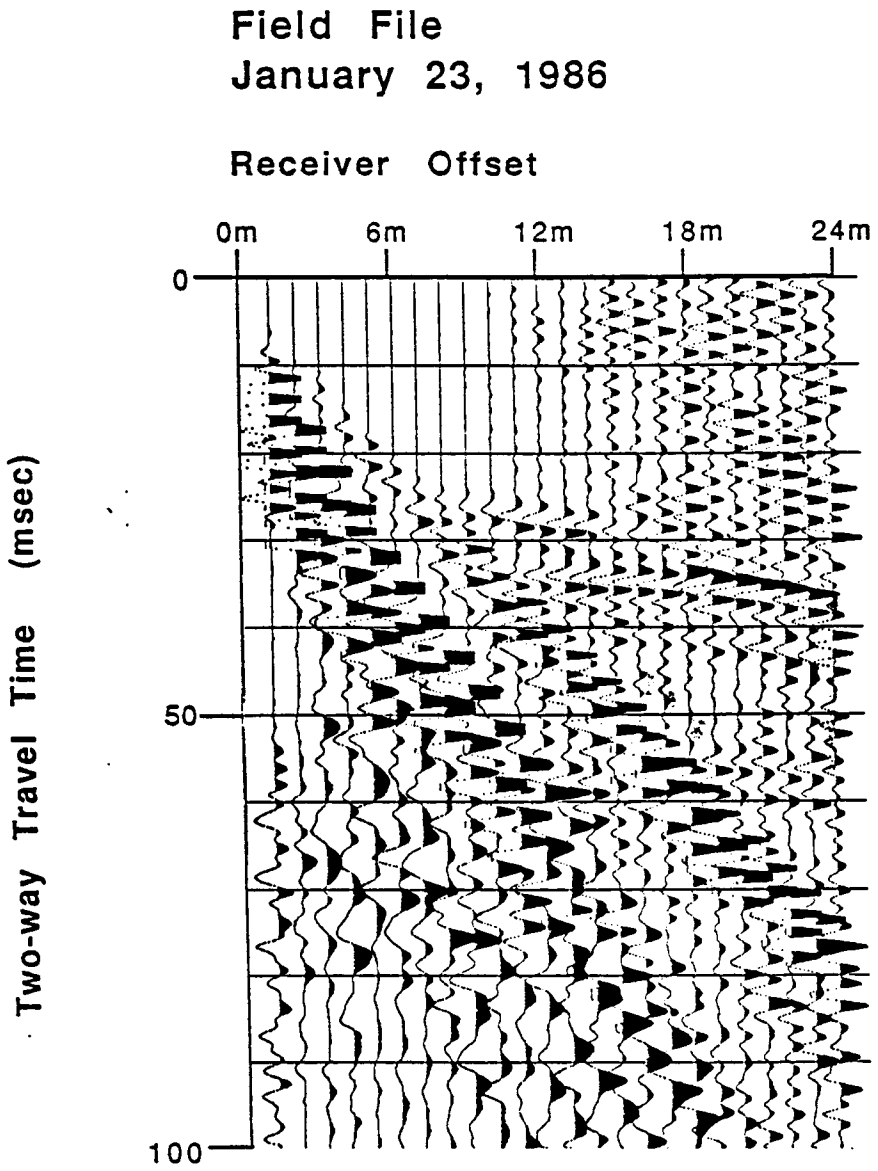

Figure 8 - Field record collected during the initial seismic reconnaissance of the pumping-test site. Reflections from within the saturated alluvium are shown in yellow. The reflection from the top of the saturated zone is present on receiver offsets of 2-4 m but is difficult to identify because the receiver interval (1 m) was too large.

if any, would be found. A shallow reflection (Figure 9) became visible on offsets of 2.5-4.5 m with this spacing. This reflection was present on the first field record but only on two or three traces which was not enough to identify it as a reflection.

The first day of testing in January had not solved all the problems so a second trip was made to the site in April, two weeks before the pumping test. The goals of this second day of testing were to remove some of the noise obscuring the shallow reflection on the inner traces and to conduct a walkaway test to identify deeper reflectors at the site. To remove additional noise on the near traces, the pre-A/D low-cut filters were changed from 480 Hz to 600 Hz and geophone dampers were installed to provide 0.6 of critical damping.

The new low-cut analog filters had 24-dB/octave rolloff below the -3 dB point of 600 Hz. Combined with the 100-Hz geophones, the 600-Hz low-cut filters removed much of the lower frequency ground roll before A/D conversion. An amplitude-versus-frequency spectrum average of two different shots demonstrates the importance of the low-cut filter (Figure 10). One was recorded with no pre-A/D filter and the second had a 600-Hz pre-A/D filter. It is obvious that the shot recorded without filtering has a higher amplitude while the shot filtered with the 600-Hz low cut has a broader bandwidth. This broad bandwidth gives a short wavelet in the time domain, a critical element of high resolution (Knapp and Steeples, 1986a,b). Little energy was recorded below 100 Hz. Applying a 600-Hz low-cut filter when the reflected signal is in the 100- to 500-Hz range removes

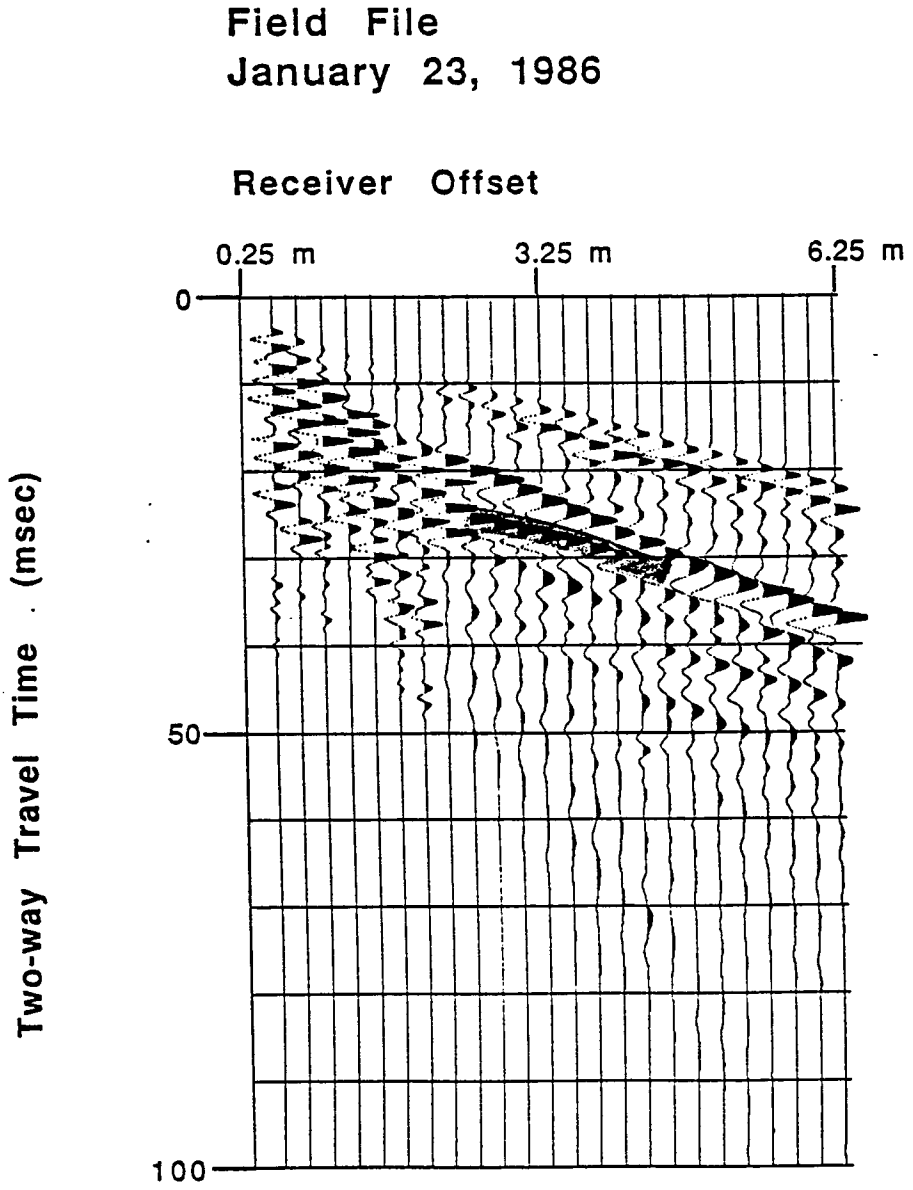

Figure 9 - Field record from the same location as the record in Figure 8. Receiver interval has been decreased to 1/4 m. The reflection from the top of the saturated zone (orange) is visible on offsets of 2.5-4.5 m.

Frequency Response Comparison of a 600-Hz Pre-A/D Low-cut Filter with No Filter

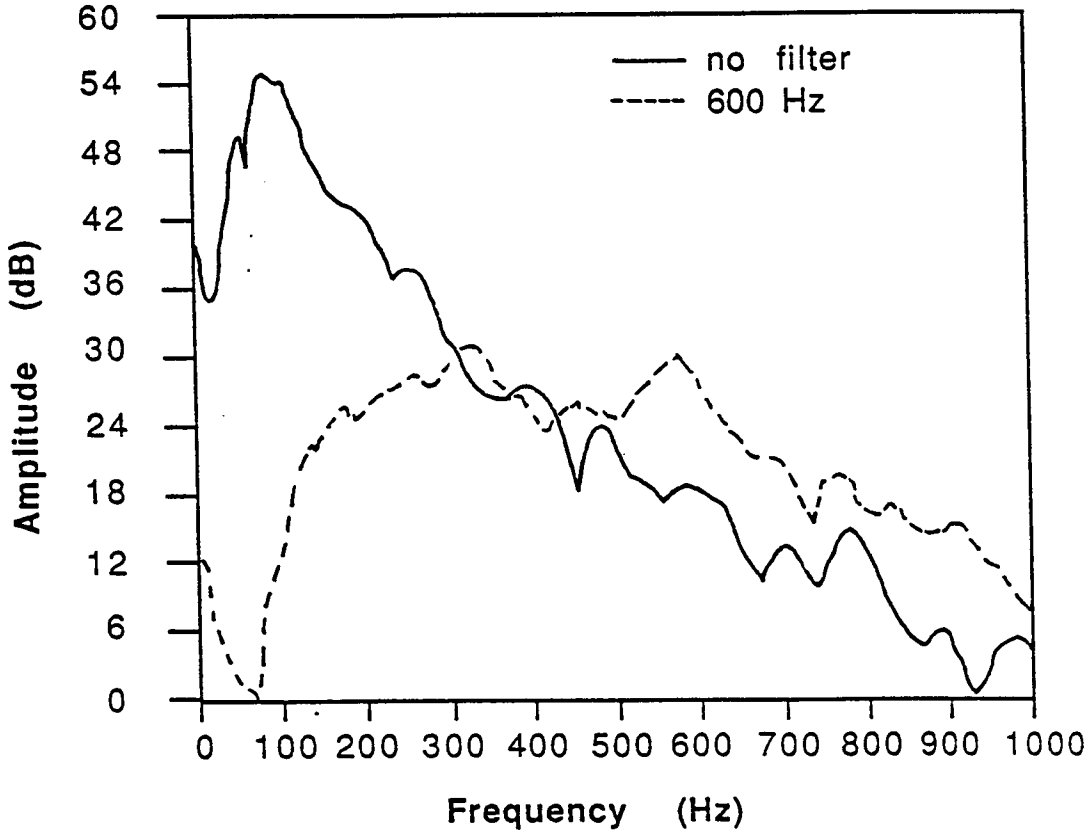

Figure 10 - Graph showing the results of removal of the low-frequency ground-roll energy by pre-A/D analog filtering. The filters remove a larger proportion of ground roll than the reflected signal so the recorded energy has a higher proportion of reflected signal. The apparent increase in energy above 400 Hz on the 600-Hz filtered data is probably due to additional air-coupled-wave energy escaping during that particular shot.

some of the signal as well as the ground roll. The important point is that the filtering removes much more ground roll than reflected signal, and the seismograph amplifier gains can be increased to compensate for the loss of signal. The end result is seismic records with most of the ground roll removed and a broad-band reflection signal recorded.

The 100-Hz geophones normally used by the KGS for shallow seismic-reflection work are undamped to increase their sensitivity in the 200-1000 Hz range. This leaves the geophones susceptible to being overdriven by energy around 100 Hz. A device was built to damp the geophones to 0.6 of critical to try to prevent overdriving of the near-source geophones by high-amplitude Rayleigh waves (ground roll). On an undamped file, traces with source-to-receiver offsets of less than 1.5 m show signs of overdriving, while with damping only traces within 0.5 m of the source show evidence of overdriving (Figure 11). Channels 18 and 19 of the file with damping were bad due to poor electrical connections within the damping device.

Much of the data from the two days of preliminary testing was collected using a split-spread geometry where the source has an equal number of recording geophones on each side (Figure 12). The source was located midway between geophone locations in what is known as half-integer offset. This particular geometry has advantages in reducing ground roll on stacked CDP sections (Knapp, 1986). End-on geometry allows easier stacking-velocity calculations and eventually was chosen for the CDP lines since the ground roll

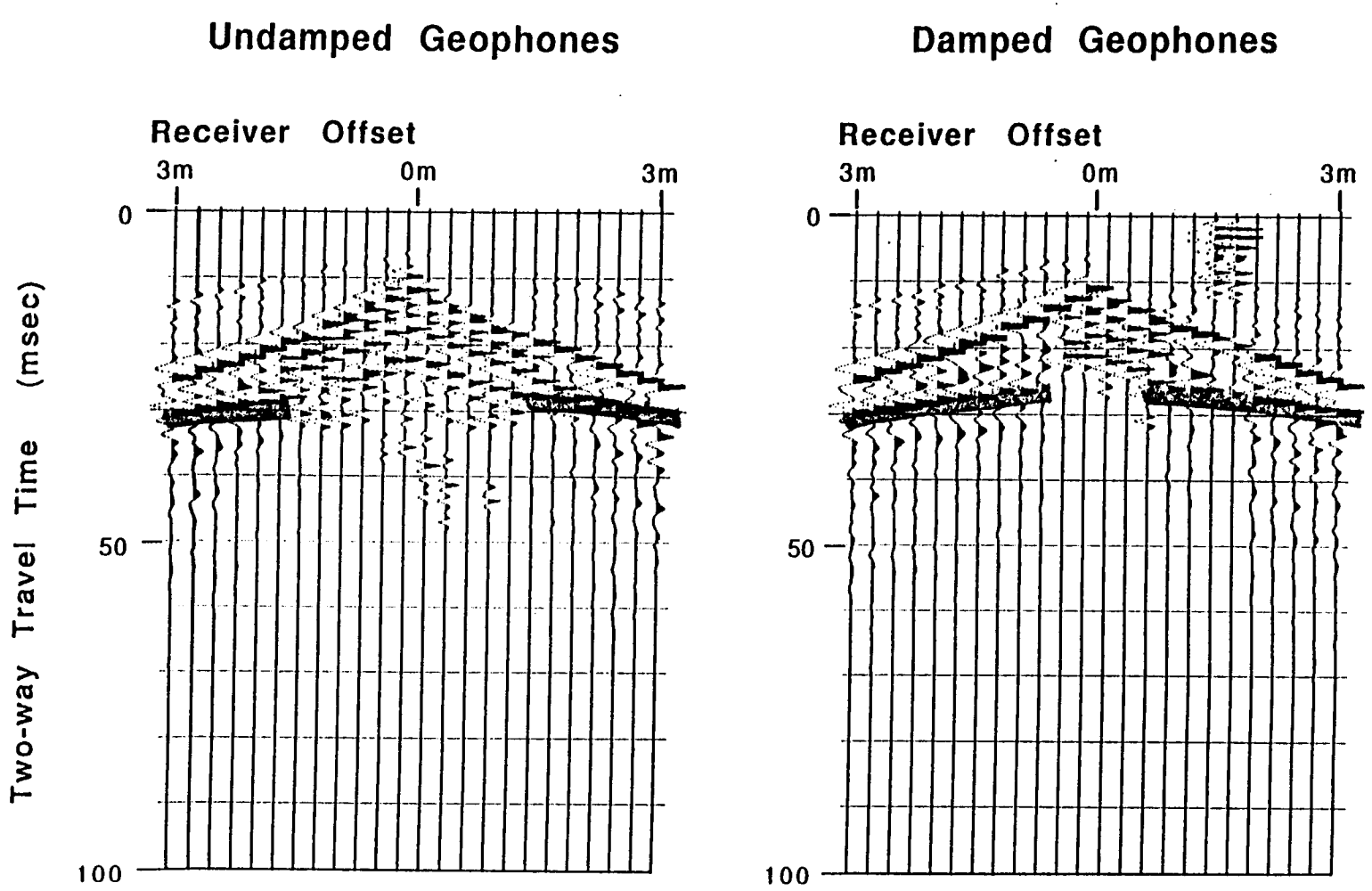

Figure 11- Geophones were damped to 0.6 of critical to prevent the close-offset geophones from being overdriven. This allowed the reflection (orange) to become visible at closer offsets.

A comparison of split-spread and end-on recording geometries

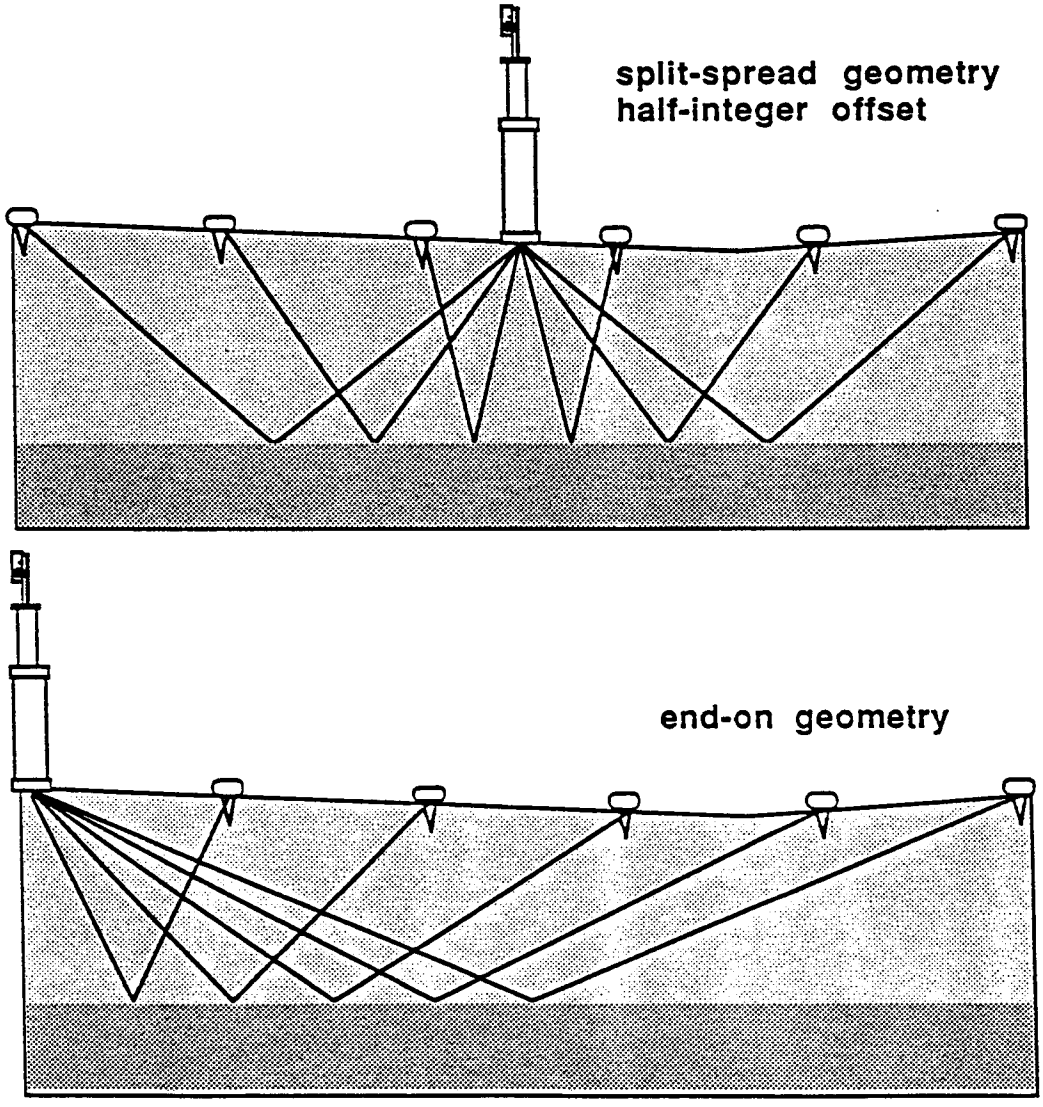

Figure 12- The split-spread geometry used had 12 live geophones on either side of the source (three shown here). The end-on geometry had all 24 live geophones on one side (five shown), which allowed more accurate velocity calculations.

was already greatly reduced from the filtering. Table 1 gives a summary of the recording parameters used.

A preliminary walkaway test was collected about 30 m south-southeast of the pumping well (Figure 13). The shallowest reflector and the target of this series of tests (A) is visible on offsets between zero and 6 m and between 20 and 30 ms in time. Two weaker reflections, presumably from clay layers, are shown by (B). The reflection from the top of the bedrock is shown by (C) and a reflection from within the bedrock is shown by (D). Arrivals from the water-table refraction (E), the air-coupled wave (F), the near-surface refracted wave (G), and the ground roll (H) are clearly visible. The optimum-window offset (Hunter et al., 1984) used for the CDP lines is also marked. The air-coupled wave and the ground roll obscure the deeper reflectors at times greater than 30 msec on the 0-6-m offsets used. The CDP lines could have been shot using different offsets to see either the shallow reflector or the deeper reflectors, but not both with a single survey using the given geometries and a 24-channel seismograph. Note also that the velocity of the unsaturated sediments was less than the velocity of sound in air, hence the first arrival in the near offsets was the air-coupled wave.

Analysis of Field Data

Four lines were shot in conjunction with the pumping test. One was shot on April 17, four days before the pumping started. The second was shot on April 24, three days after the pumping started.

Recording Parameters

Seismograph:	Input/Output DHR 2400 24 channels Fixed gain 11-bit + sign A/D conversion 500 samples 1/4-millisecond sample interval 125-millisecond record length 600-Hz pre-A/D low-cut filter 24-dB/octave rolloff 1500-Hz anti-alias high-cut filter 60-dB/octave rolloff
Source:	Single 180-grain bullet from a silenced 30.06 rifle
Receivers:	Single Mark Products 100-Hz geophones Damped to 0.6 of critical 1/4-meter group interval 1/4-meter source-near receiver offset 6-meter source-furthest receiver offset End-on geometry

Table 1.

Figure 13 - Walkaway test with interpretation identifying the major seismic arrivals. The target reflector is the top of the saturated zone (A). Other arrivals visible are reflections from clay layers in the alluvium (B), top of the bedrock surface (C), a boundary within the bedrock (D), as well as the refraction from the saturated zone (E), the air-coupled wave (F), and the near-surface refraction (G). The stippled area (H) is predominately surface waves.

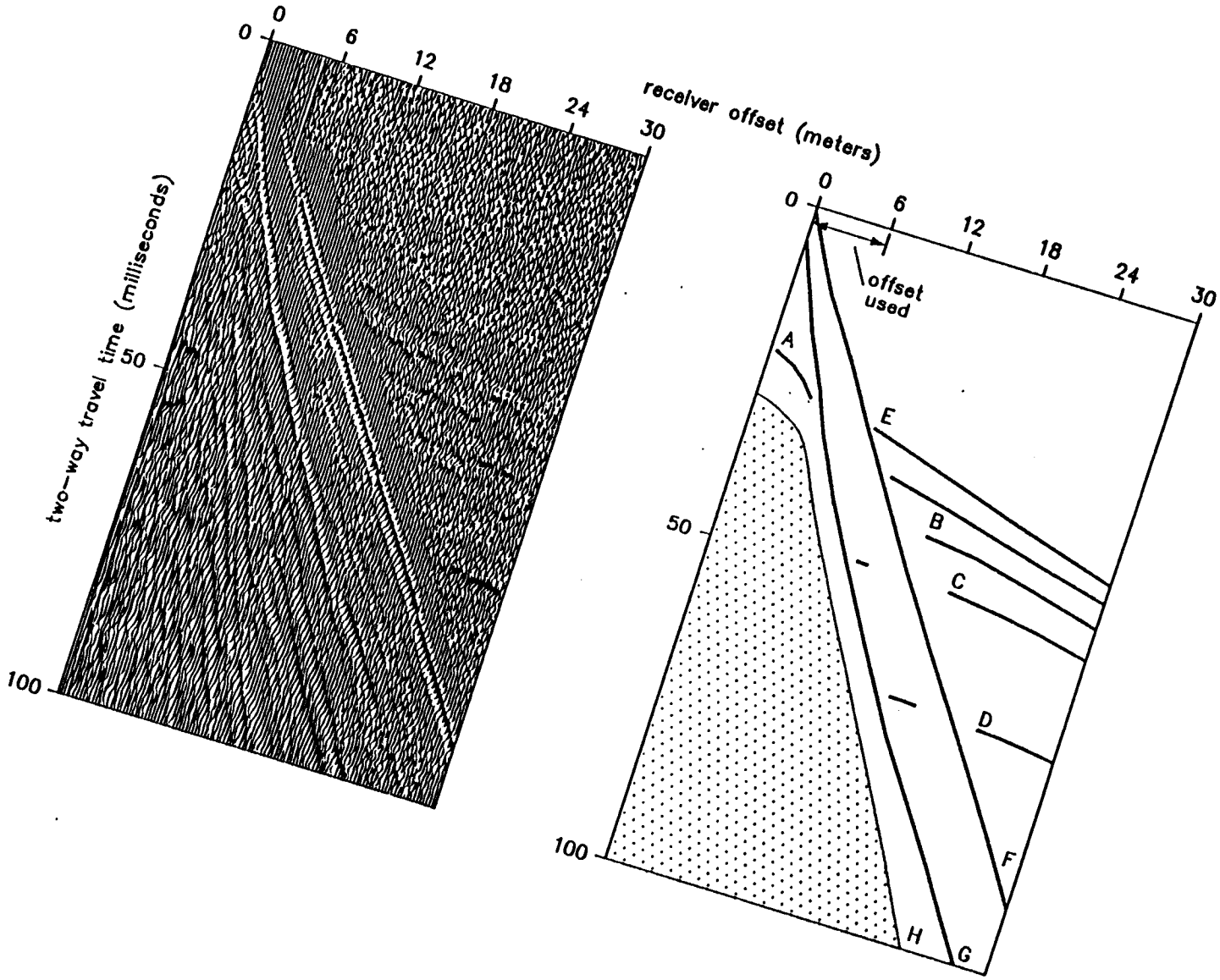
0
0
6
12
18
24
30
receiver offset (meters)
two-way travel time (milliseconds)
50
100
offset used
A
E
B
C
D
F
G
H

The third line was shot on April 28, after seven days of pumping, the time of maximum drawdown. A fourth line was shot on April 29, just after the pump was turned off, during the time of the maximum rate of recovery. A final line was shot on August 14 to check the reproducibility of the results over an extended period of time.

The bulk of the results came from the four lines shot in April during the pumping test. The geophones were left in place for the duration of the pumping test so all four lines could be collected with no change in the near-surface receiver conditions. Any changes from one line to the next were from the changing hydrologic conditions, including rainfall, and minor source variations. The line of geophones extended from the neutron-probe access tube, linearly away from the pumping well, to 4 m beyond the 100W observation well (Figure 2). Subsurface coverage ranged approximately from 1 m southeast of the neutron-probe access tube to the 100W observation well, covering a major portion of the expected change in water level.

Example field files from each of the four CDP lines shot during the pumping test show a downward shift in time of the reflection on the second, third, and fourth files when compared to the first file (Figure 14). The reflection has a zero-offset time of 22.5 msec on the April 17th file, 23.4 msec on the April 24th file, 24.5 msec on the April 28th file, and 25.3 msec on the April 29th file. Depth calculations based on the normal moveout (NMO) of the reflectors give depths of 2.7 m for the first file, 3.0 m for the second file, 3.0 m for the third file, and 3.0 m for the fourth file. These

Figure 14 - Field records from the same location (CDP 266) with the reflection (orange) the direct/near-surface refracted wave (yellow), and the air-coupled wave (blue) identified. Notice the downward shift in time of the reflection during the pumping test.

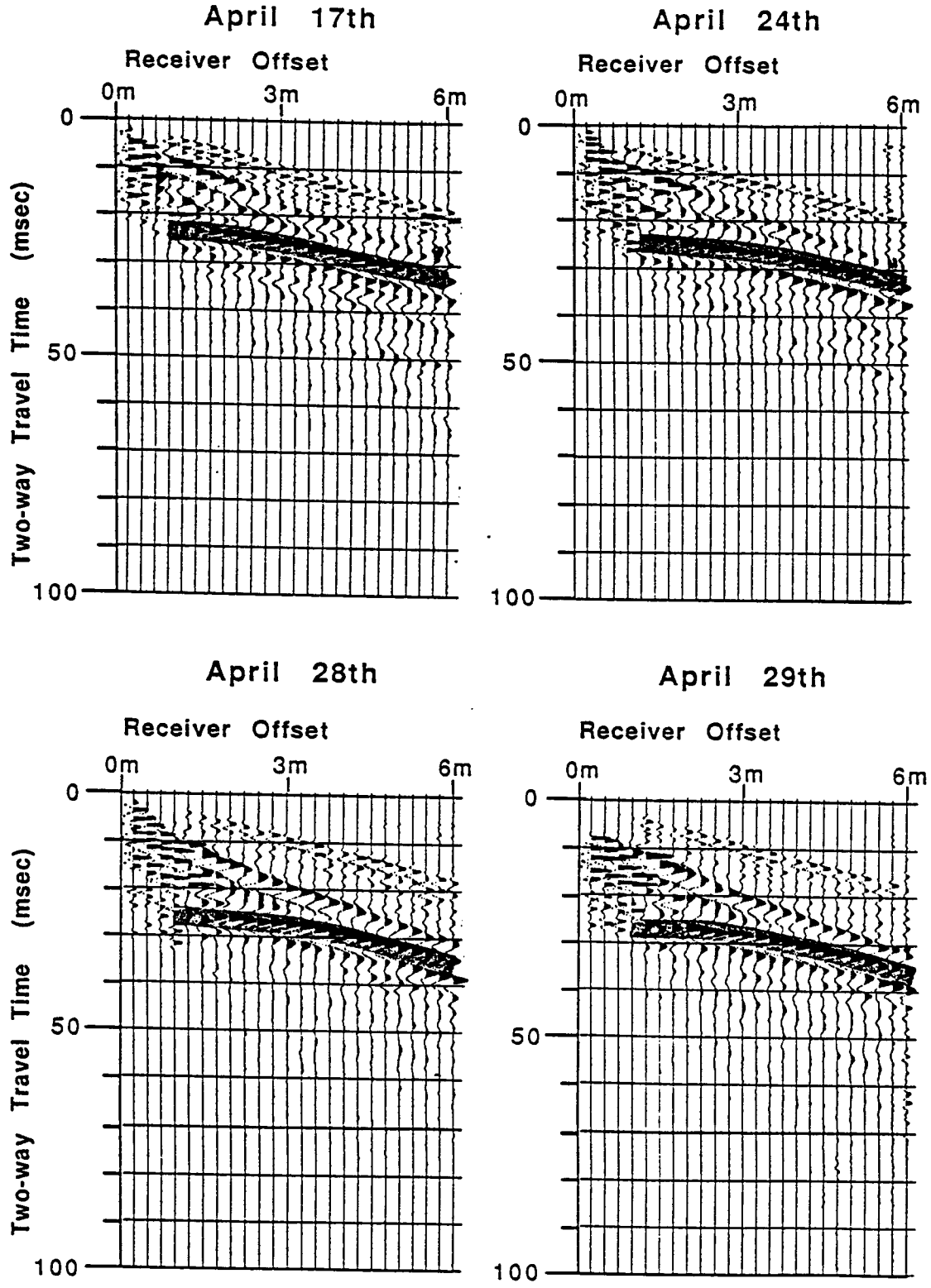
April 17th
Receiver Offset
0m
3m
6m
0
50
100
Two-way Travel Time (msec)
April 24th
Receiver Offset
0m
3m
6m
0
50
100
April 28th
Receiver Offset
0m
3m
6m
0
50
100
Two-way Travel Time (msec)
April 29th
Receiver Offset
0m
3m
6m
0
50
100

depth calculations are for a single point along the seismic lines and are not the average values across the entire lines. The calculated stacking velocity at that point changed over the course of the test for reasons discussed later. The reflection is the strongest coherent event on the records. Beneath the reflection, the first primary multiple reflection is visible on the first file at about double the zero-offset intercept time for the reflection.

An amplitude-versus-frequency spectrum of a single trace has peaks that can be identified according to the type of seismic energy primarily responsible for the peak (Figure 15). The most obvious peaks correspond to the direct/refracted wave and the reflected wave. There is a conspicuous lack of energy below 150 Hz where the large-amplitude ground-roll energy would be, had it not been removed by the severe low-cut filtering mentioned earlier.

The amplitude-versus-frequency spectra of the reflected wavelets, before pumping and at maximum drawdown, were obtained by averaging the spectrum of the reflected wavelet from a single channel with a source-to-receiver offset of 2.5 m for six consecutive shot points. The prepumping spectrum has a higher dominant frequency and a broader bandwidth than the maximum-drawdown spectrum (Figure 16). This effect would be expected if the acoustical boundary causing the reflection became more diffuse after the pumping started. This illustrates, in the frequency domain, the difference that is visible in the time domain on the field records between the reflected wavelet before pumping and the reflected wavelet at maximum drawdown.

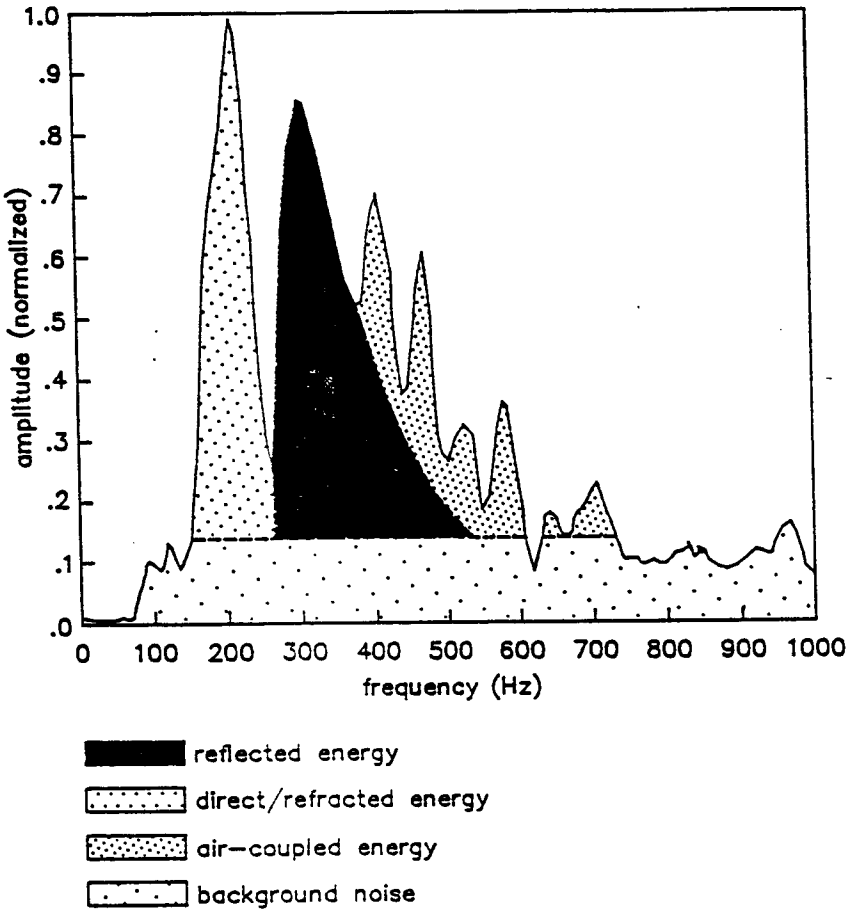

Figure 15 - Amplitude-versus-frequency spectrum of a single trace with the major energy peaks identified. Background noise is a combination of instrument and ambient ground noise.

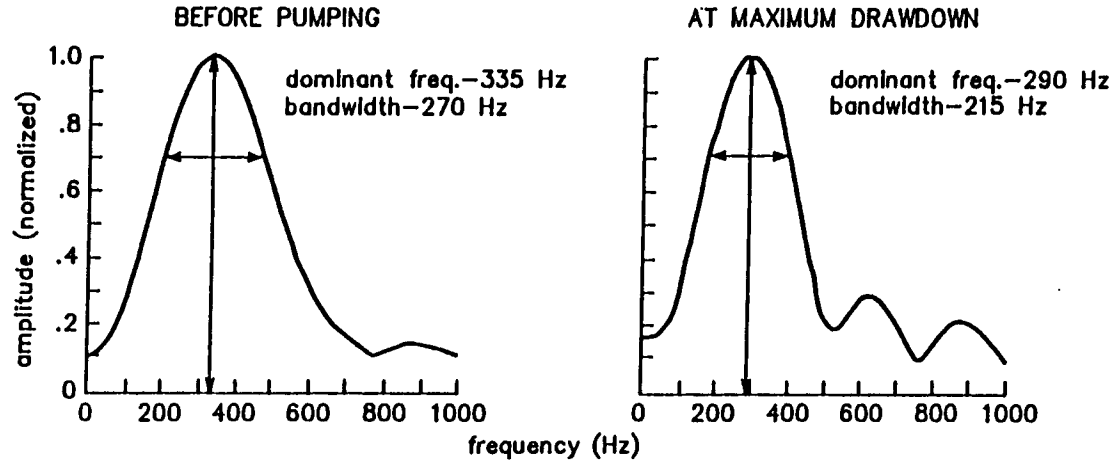

Figure 16 - Amplitude-versus-frequency spectra of the reflected wavelet. Each spectrum is the average of the reflected wavelet from a single channel at 2.5-m offset for six consecutive shot points. The spectrum before pumping has a higher dominant frequency and a broader bandwidth than the spectrum at maximum drawdown.

Results

The remaining analyses of the data concentrated on answering four questions:

(1) What was the exact nature of the shallow reflecting surface seen on the field records?

(2) Could the data collected targeting the shallow reflector be used to image the clay layers in the alluvium?

(3) What caused the humps in the shallow reflection that were visible on the CDP sections?

(4) Is there any information contained in the calculated stacking velocities and correlation coefficients that could characterize the sediment above the reflector?

Processing of the data was done in two phases. Relatively simple processing was done to supply information on depth to the reflector, drop of the reflector as the pumping test continued, and the shape of the reflecting surface. After a general understanding was reached about what was happening geologically and hydrologically, a series of more complicated processing steps was performed on the data to try to enhance the topography of the reflector as well as to make any underlying clay layers visible (Figure 17).

Shallow Reflection

The results from the simple processing sequence were excellent due to the strength of the target reflector and the first primary

Processing Steps	Explanation
Preparation of data for processing	Field tapes are read into the Data General MV 20000 computer and put into a format that the processing software can read.
Editing bad traces	Traces with little or no reflection information are deleted.
Time-break correction	Shot static corrections are applied to uniformly align each field file. Shot statics are based on the air-coupled wave arrival.
CDP sort	Data are sorted into groups containing traces with the same source-to-receiver midpoint (CDP).
Normal-moveout correction	NMO stacking velocities are calculated and applied to line up the reflected wavelet in a straight line across the CDP gather.
Surface-consistent static correction (AUTS)	Surface-consistent statics are calculated and applied to the data to remove the effects of slight velocity anomalies at a given receiver or shot location.
CDP stack	All the traces in a CDP gather are summed to form a single trace per CDP.
Automatic gain-control scaling	Automatic gain-control scaling is applied to the CDP traces to enhance the weaker signals further down in time on the traces.

Figure 17 - CDP-processing steps and their explanation.

multiple reflection. For the simple processing, a constant stacking velocity with time was used for two reasons. First, there were no deeper reflections visible on either the field records or in any of the subsequent analyses. Second, the constant velocity with time emphasized the multiple reflections. This was done in order to show that as the primary reflection moved down in time throughout the test, the multiple reflections moved down twice as far. This stacking velocity was allowed to vary horizontally over the length of the line because there was a change in the calculated stacking velocities across the line on the order of 20-30 m/sec. The stacking velocities are discussed in greater detail later and are shown in Figure 35 along with the velocity function applied to the data.

On the CDP section from April 17th, the shallow reflection at 22 msec has a high amplitude and is the most continuous event on the section (Figure 18). Slight humps are visible in the shallow reflection at CDPs 220-240, 296-305, and again at 330-338. The strong amplitude event at 46 msec is at twice the time and stacks in at the same velocity, suggesting that it is the first primary multiple reflection. A second event at 70 msec appears to be a second multiple reflection while there is a hint of a third multiple reflection around 90 msec.

The CDP section from the line collected on April 24th shows the shallow reflection has dropped to about 24 msec, corresponding to an average depth of about 2.9 m (Figure 19). In addition, the humps in the reflection observed on the April 17th data are much less

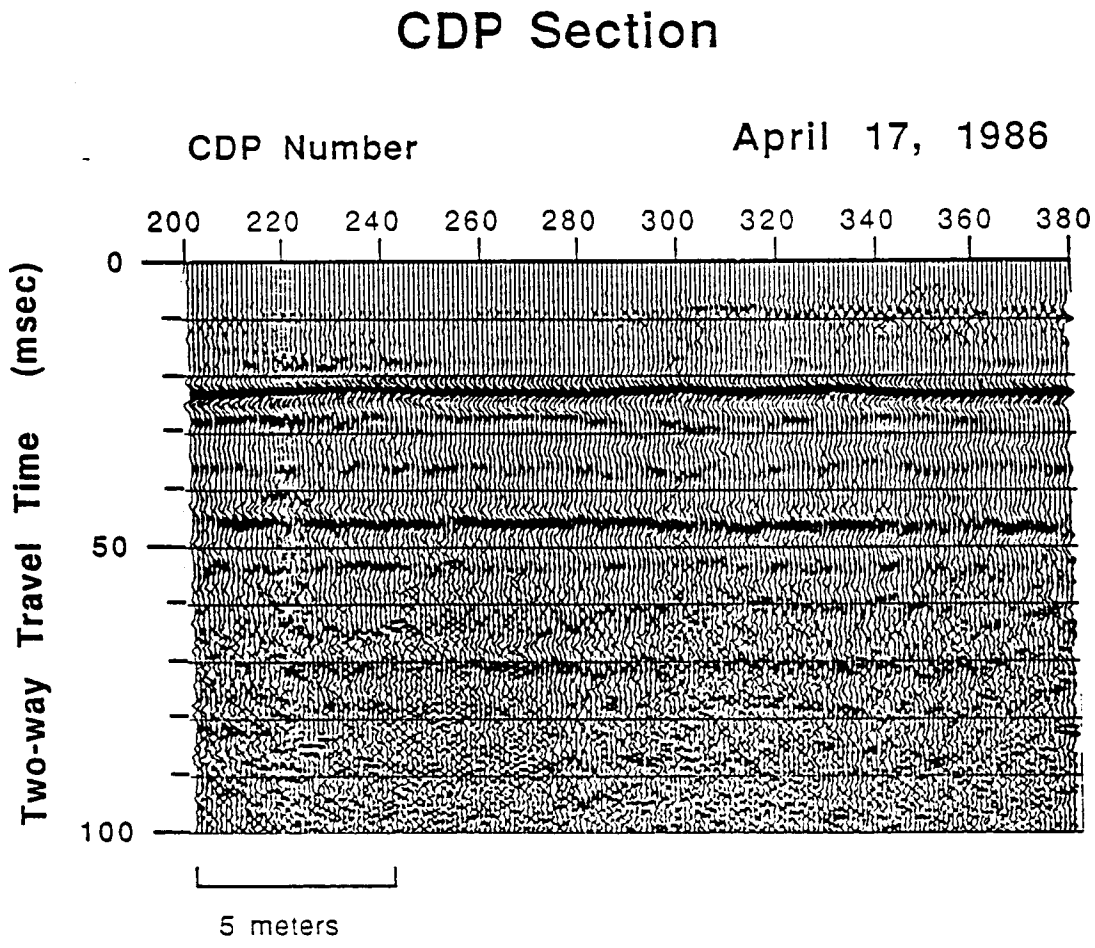

Figure 18 - CDP section collected before pumping began showing the reflection from the top of the saturated zone (orange) at 22 msec and two surface multiple reflections (green). Slight humps in the reflection at CDPs 220-240, 296-305, and 330-338 may indicate finer-grained sediments.

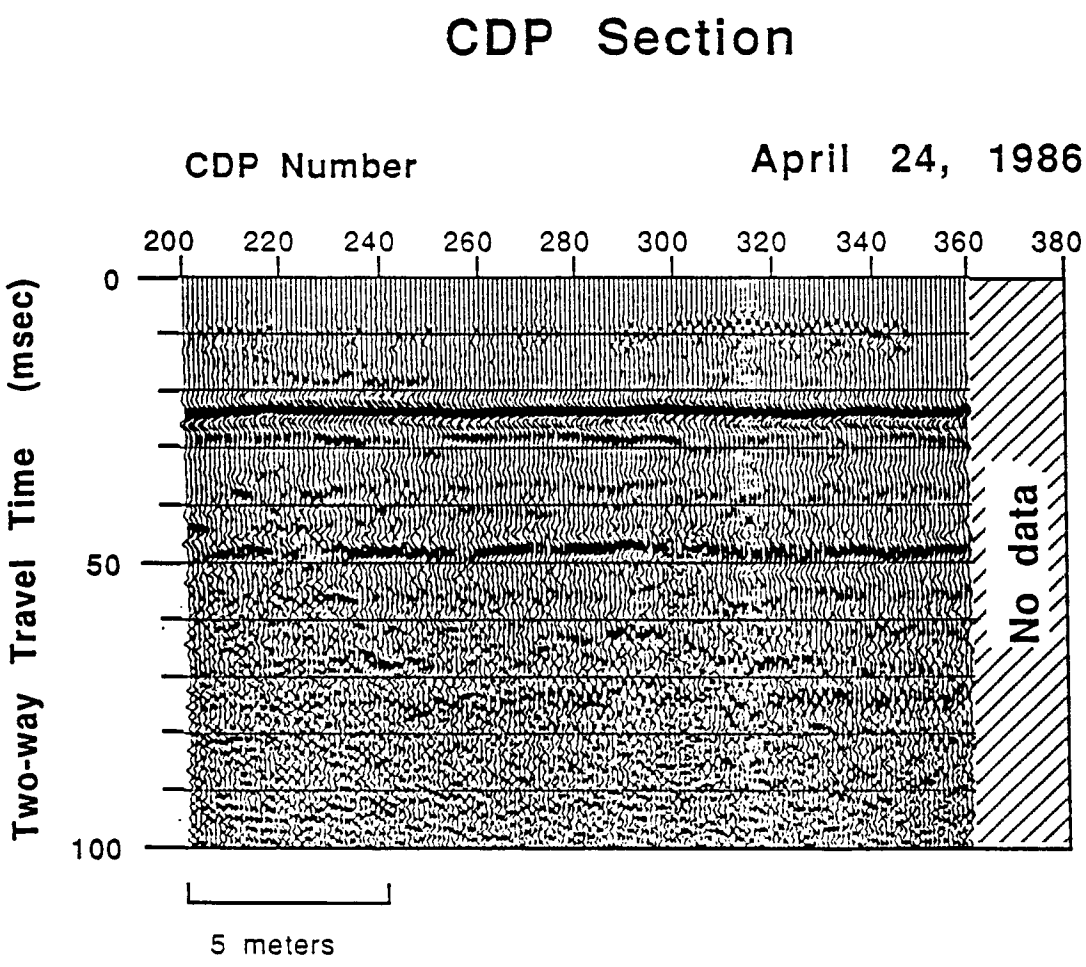

Figure 19 - CDP section collected three days into the pumping test. The reflection (orange) has shifted down in time to 24 msec and the multiple reflections (green) are noticeably weaker than those in Figure 18. The humps previously observed are beginning to flatten.

pronounced. The other changes from the April 17th section are that the first multiple reflection, at 48 msec, is lower in amplitude and less continuous than its counterpart on the first section, and the second multiple reflection is barely noticeable at 72 msec.

The April 28th CDP section, collected at maximum drawdown, shows the shallow reflection has dropped to about 26 msec, corresponding to a depth of approximately 3.1 m, and the previously observed humps in the reflection have disappeared (Figure 20). The first multiple reflection has dropped to 51 msec with similar amplitude and wavelet character as the first multiple reflection observed on the April 24th CDP section.

The neutron-probe data collected during the pumping test were used as a reference to try to determine if the strong acoustical boundary seen on the seismic data was a hydrologic boundary. The neutron probe shows the percentage of water per total unit volume present at a given depth in an aquifer. For example, for a sand with 30% porosity that was fully saturated, the neutron-probe data would show a moisture content of 0.30. That same sand with a uniform 1/3 saturation would show as 0.10 on the neutron probe. By taking saturation readings at regular depth intervals, moisture profiles of the near-surface sediments were constructed.

The neutron-probe data were collected on April 19th, 24th, and 28th at CDP 202 (Figure 21). Plotted along with the neutron-probe data are the calculated depths to the reflecting interface from the seismic data at CDP 202 and the water level at CDP 202 interpolated from measurements in the observation wells. On all three curves,

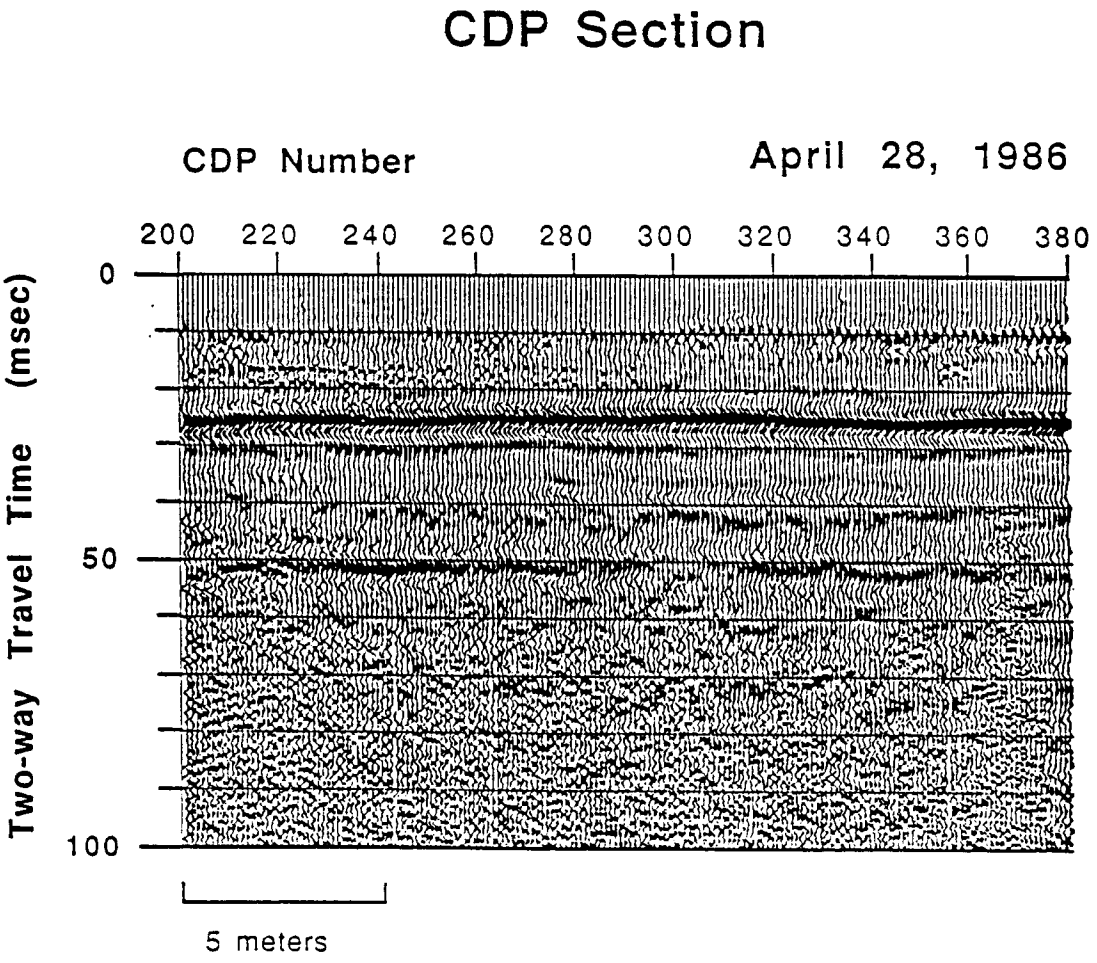

Figure 20 - CDP section collected at maximum drawdown. The reflection (orange) has dropped to about 26 msec and does not have the pronounced humps seen previously in Figure 18. The first multiple reflection (green) is weaker than in Figures 18 or 19 and the second multiple reflection has disappeared.

Figure 21- Moisture profiles from neutron-probe data, reflecting interface from seismic data and water levels interpolated from observation wells. On all three dates, the top of the saturated zone from the moisture profiles correlated well with the seismic-reflector depth. The water level from the observation wells correlated only before pumping, suggesting that on the short term, the upper portion of the aquifer acted as a separate unit from the lower portion.

Moisture Profiles

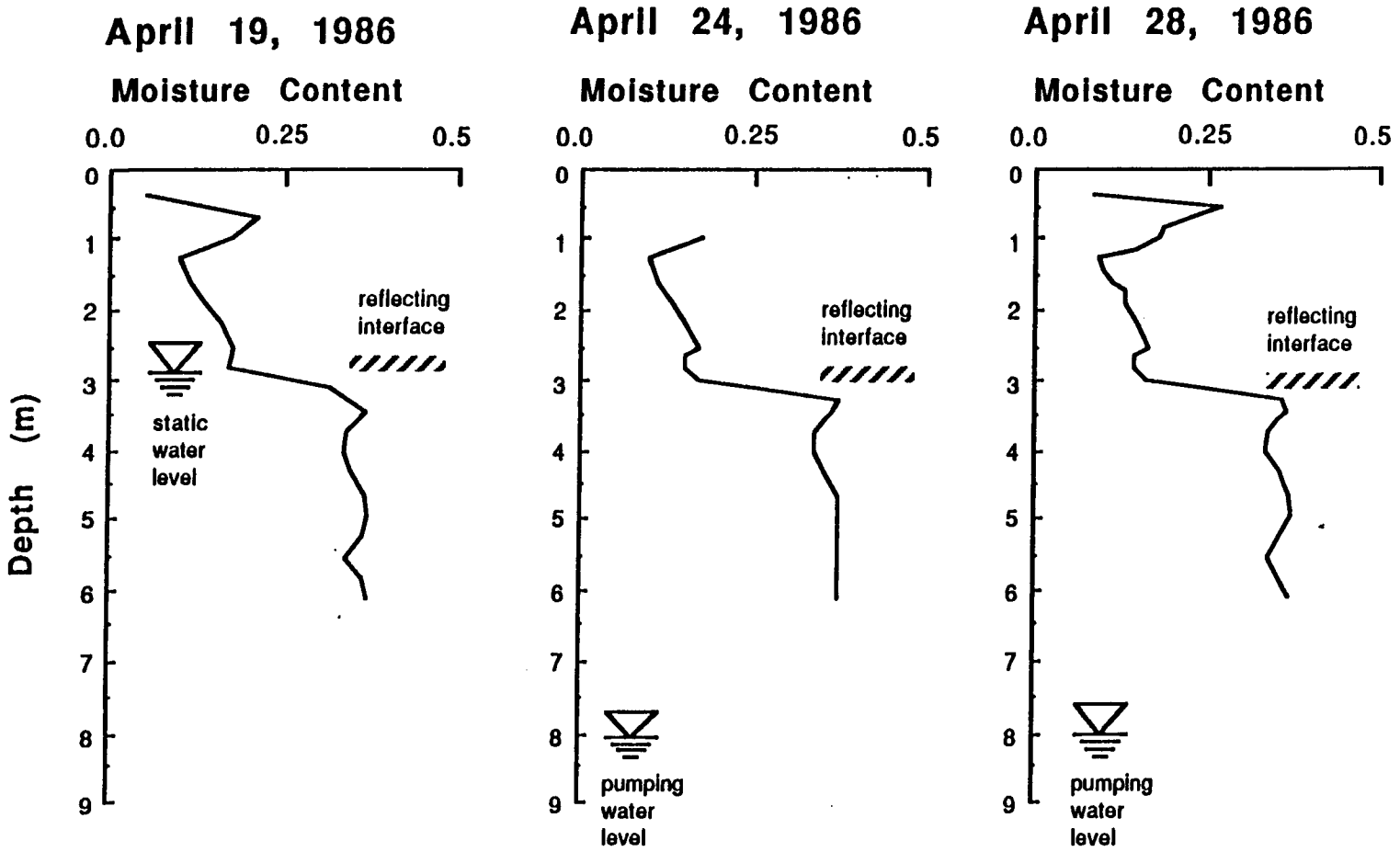

the reflector depth correlates extremely well with the depth where the moisture profiles show a large, rapid increase in water content. This correlation between reflector depth and the top of the fully saturated sediment is expected since the presence of water greatly influences both the velocity and the density (the two parameters that determine reflection coefficients) of the unconsolidated aquifer. The April 17th seismic line was collected two days before the installation of the neutron probe so the closest comparison possible was the April 19th neutron-probe data. Since the static water level matched the neutron-probe and seismic data very closely, the comparison is probably valid.

When the pumping started, the water level in the wells fell 2.5-5 m in the same time the water level based on the neutron-probe and seismic data showed a drop of about 0.5 m. The first explanation developed for this was that the water in the aquifer between the top of the saturated zone and the pumping level was held in place by surface tension and that this water was slowly draining as a delayed-yield volume. This explained why the seismic and the neutron-probe data correlated well and water levels from the observation wells did not. This interpretation presented several problems that became apparent as the analyses continued. First, the lithology of the aquifer was predominantly coarse sand and gravel making it a very transmissive aquifer (Sophocloeus et al., 1987) and not conducive to retaining these large volumes of water in the pore spaces above the water table. Second, the seismic sections show no indication of any cone of depression.

Correlating the data from seismology, neutron probe, and observation wells became more difficult with the data collected on April 29th. Assuming the observed reflection was from the top of the saturated zone, these data should have recorded the rise of the water table from pumping levels back to the original static levels. When these data were processed, they looked nearly identical to the data collected the day before (Figure 22). The neutron-probe data from April 29th also remained virtually identical to the data from the day before. This was unexpected because the water level in the observation well, 100W, rose over 2 m during the 30 minutes it took to shoot the line. No recovery effects were seen in the seismic or neutron-probe data.

On August 14, 1986, a final CDP line was collected at the pumping-test site to see if similar results could be obtained after an extended period of time. The date in August was chosen because late summer is the end of the normal irrigation season, when the lowest aquifer water levels are expected. Heavy rainstorms hit the area a few weeks before the experiment and consequently, the water table was higher than expected, averaging about 3.1 m below the land surface. The saturated-zone reflection is very flat and uniform across the section (Figure 23). The hump at CDPs 370-380 was a product of geophones planted in higher-velocity material near the 100W observation well. The neutron-probe data give a depth of 2.9 m which compares to 3.0 m, the calculated depth from the seismic data at CDP 202.

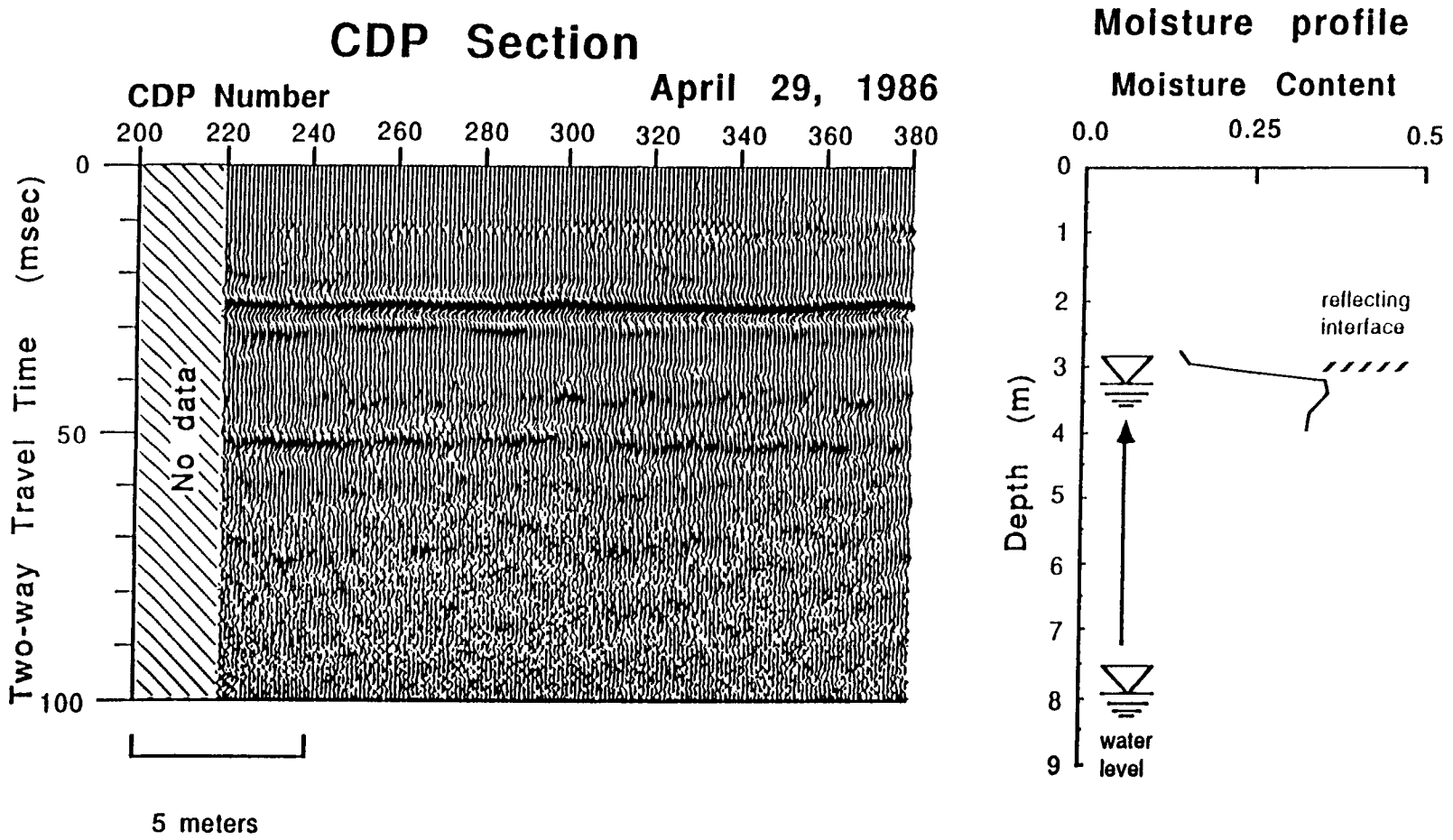

Figure 22 - CDP section collected just after the pump was turned off. The reflection (orange) and multiple reflection (green) appear almost identical to those at maximum drawdown (Figure 20). The changing obsevation-well water levels did not appear to affect the seismic or the neutron-probe data.

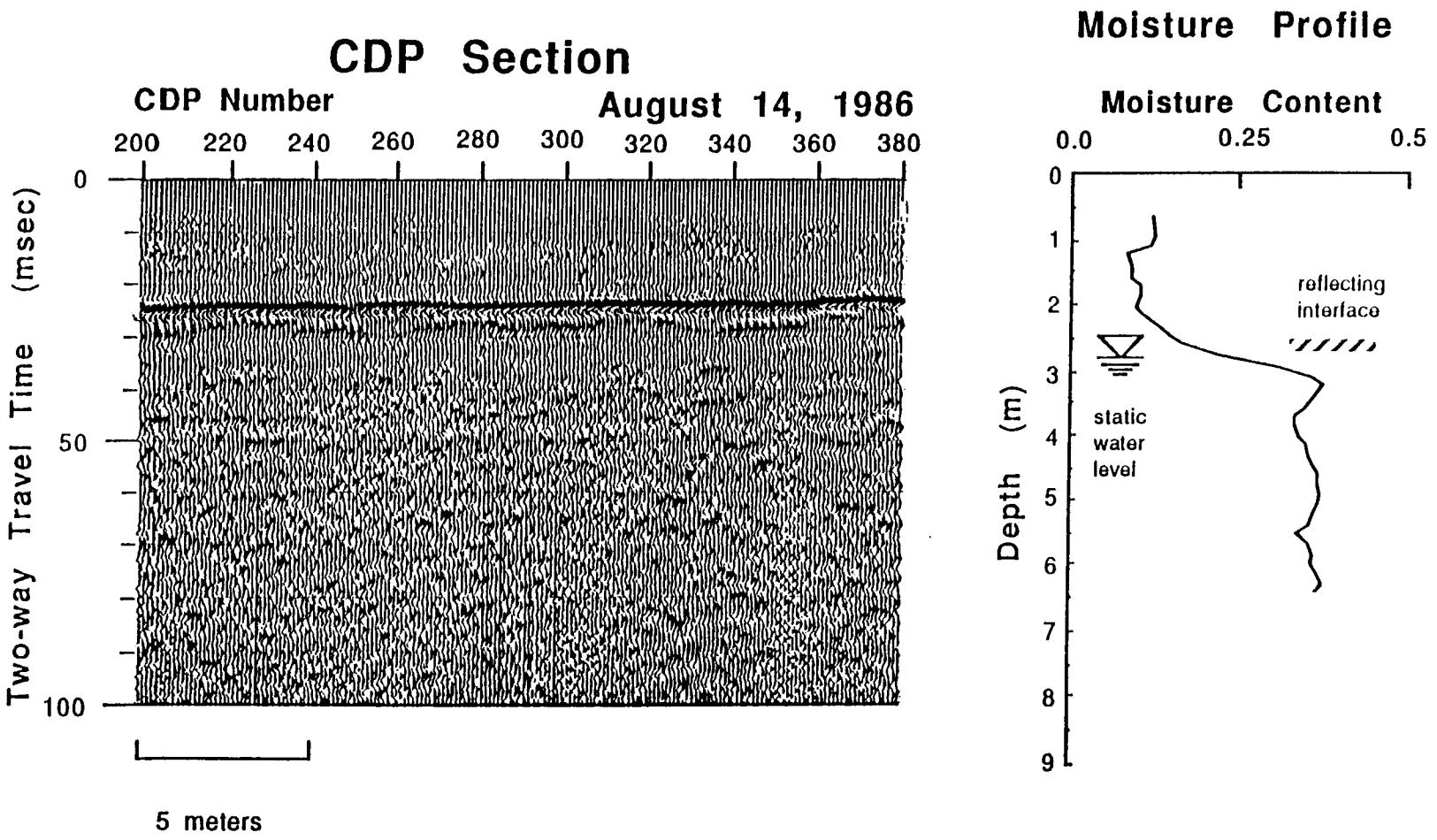

Figure 23 - CDP section collected four months after the pumping test to check results over a long period of time. As before, under nonpumping conditions, the top of the saturated zone, seismic reflector, and the observation-well water levels are at the same depth.

The elevation of the reflector below ground surface was calculated from the CDP gathers using a Hewlett-Packard HP-11C hand calculator and a program from Steeples and Miller (1986). The program takes reflection times picked at various offsets from the unstacked CDP gathers and does a least-squares fit to a hyperbola. It then calculates NMO stacking velocity, zero-offset intercept time, depth to the reflector, and a correlation coefficient showing how close the points come to the calculated line. The values graphed, calculated for even-numbered CDPs, tend to fluctuate about the dotted line which is interpreted as the true reflecting surface (Figure 24). The scatter of the values about this line represent error from near-surface velocity changes and from inaccurate time readings. The reflecting surface clearly drops from an average value of 2.7 m to 3.2 m over the course of the pumping test.

The corrected interpretation (Figure 25), reinforced by subsequent gamma-ray logs of the observation wells, is that a clay layer, 10-13 m below the ground surface, is continuous enough over the pumping-test site to act as a semi-confining layer. This layer causes the upper 10 m to act as a perched aquifer in the vicinity of the pumping well. The water in this upper part slowly drains through (or around) the clay layer causing a much slower drop in the saturated zone than expected. The seismic data, which image the top of the saturated zone, record this slowly falling surface. The saturated zone drops to the elevation of the river and then stabilizes as a relatively flat surface with no cone of depression.

Figure 24 - Graphs of the elevation (below ground surface) of the seismic reflector (solid line) and the interpreted reflecting surface (dotted line). Discrepancies between the two lines are due to near-surface velocity changes and inaccuracies in the time measurements.

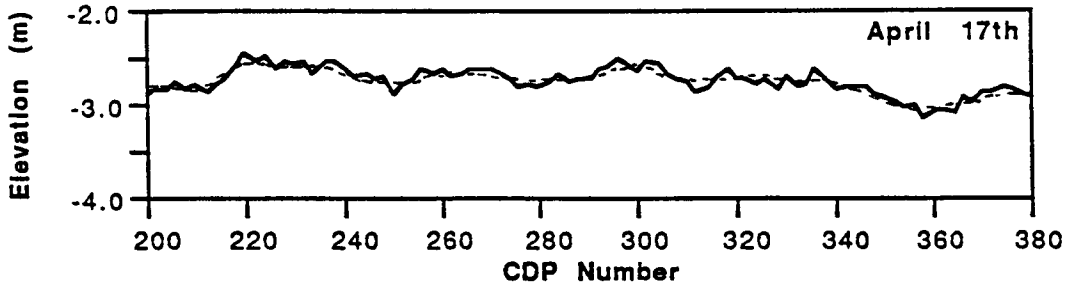
April 17th
Elevation (m)
-2.0
-3.0
-4.0
200 220 240 260 280 300 320 340 360 380
CDP Number

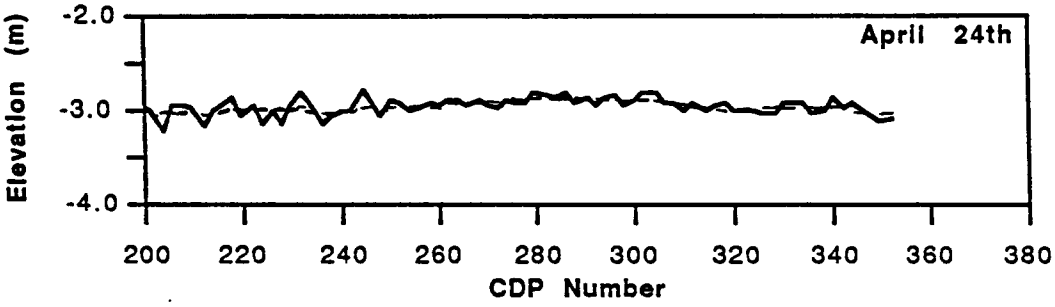
April 24th
Elevation (m)
-2.0
-3.0
-4.0
200 220 240 260 280 300 320 340 360 380
CDP Number

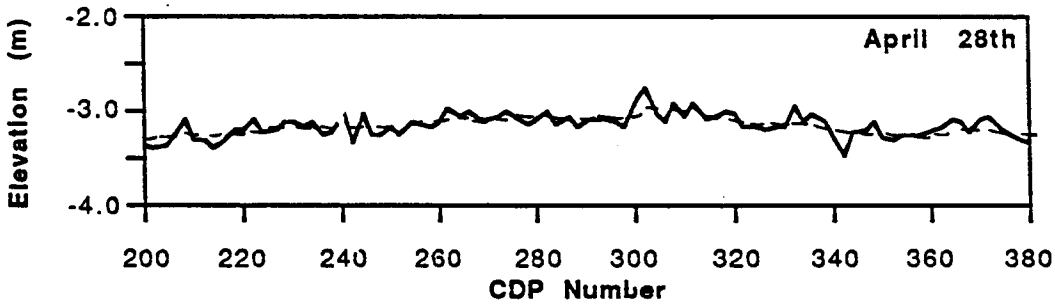
April 28th
Elevation (m)
-2.0
-3.0
-4.0
200 220 240 260 280 300 320 340 360 380
CDP Number

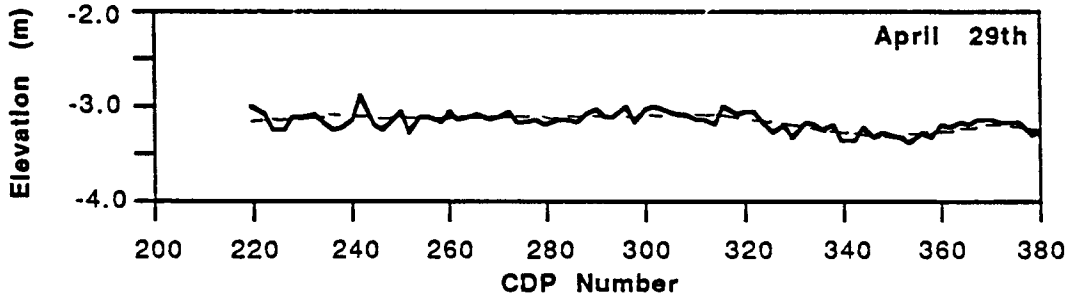
April 29th
Elevation (m)
-2.0
-3.0
-4.0
200 220 240 260 280 300 320 340 360 380
CDP Number

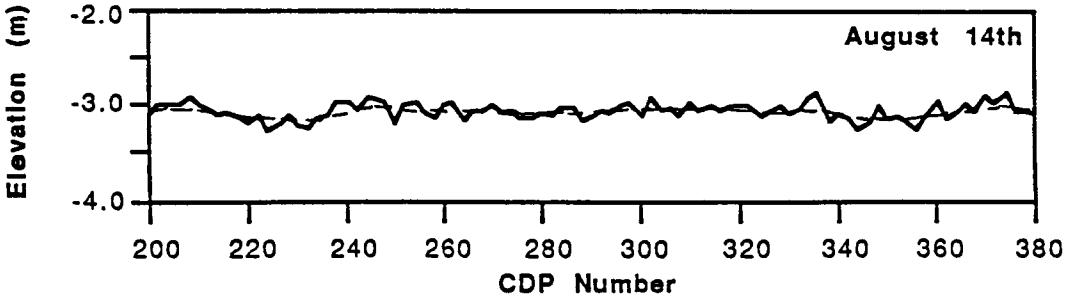
August 14th
Elevation (m)
-2.0
-3.0
-4.0
200 220 240 260 280 300 320 340 360 380
CDP Number

Figure 25 - Interpretation of flow patterns at the pumping-test site during pumping. The intermediate clay layer created a perched water table causing the upper and lower portions of the aquifer to function as separate aquifers over the time scale of the test. All of the observation wells were screened below the clay layer so their water levels were not necessarily indicative of the short-term changes in water level above the clay layer.

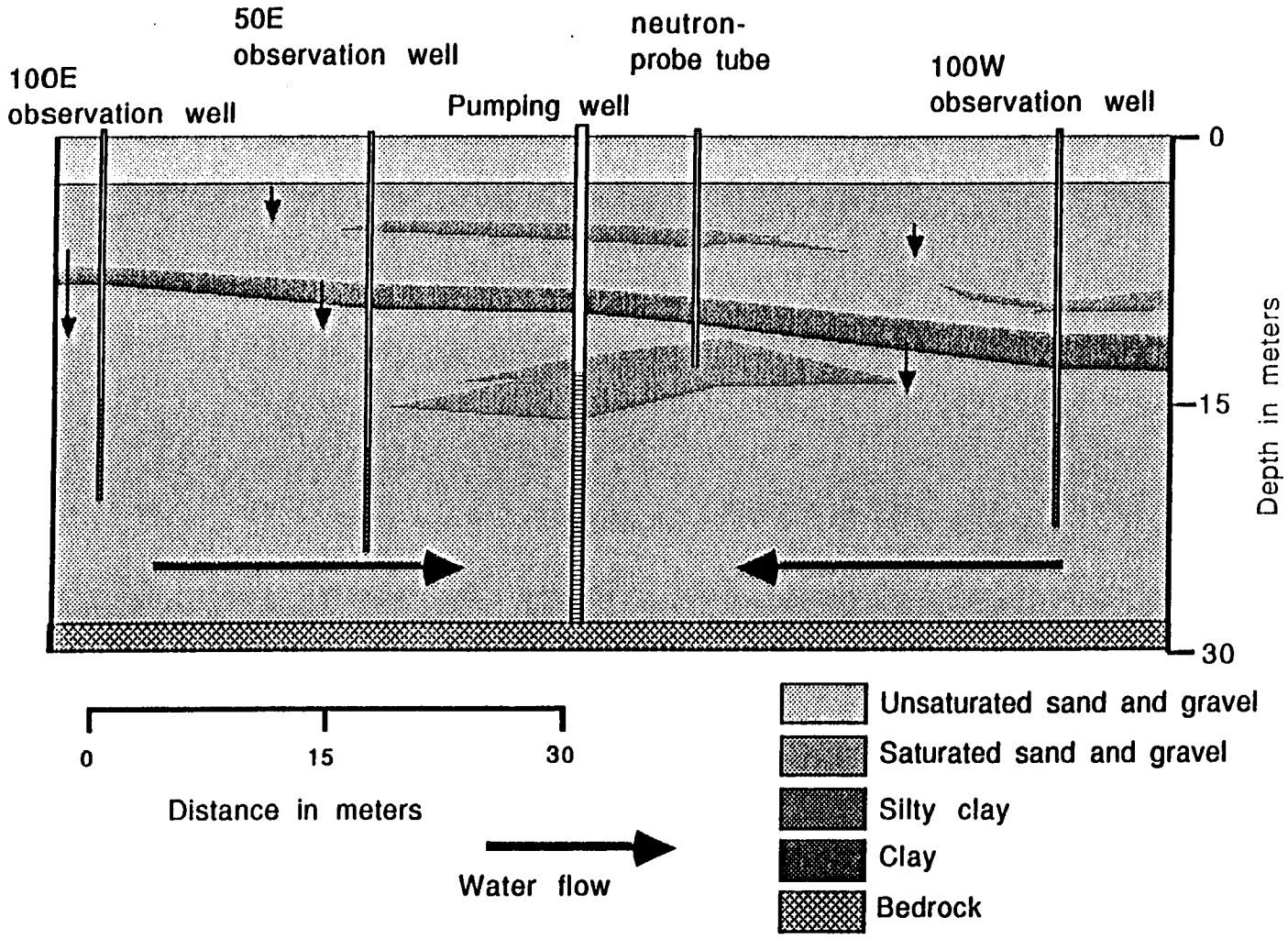
50E
observation well
neutron-
probe tube
100E
observation well
Pumping well
100W
observation well
0
15
30
Depth in meters
0
15
30
Distance in meters
Water flow
Unsaturated sand and gravel
Saturated sand and gravel
Silty clay
Clay
Bedrock

Conversely, the clay layer also acts as a lid, preventing the water from rising quickly into the upper portion from below.

Additional Processing

The semi-confining layer was an important part of the interpretation, but reflections from the clay layers within the alluvium were obscured by ground roll on the source-to-receiver offsets used (see Figure 13). Additional processing steps were performed to try to make any clay-layer reflections visible on the CDP sections (Figures 26 and 27). In addition to these final sections (Figures 28 to 32), the data were stacked at the higher velocities at which the clay layers would have coherently stacked if they were present in the data (CDP sections not shown). These velocities were based on the calculated stacking velocities of the reflections from the clay layers on the walkaway test. Unfortunately, the clay layers visible on the walkaway test did not show up at the higher NMO stacking velocities, leading to the conclusion the signal from these layers was too weak to record through the noise.

The deconvolution was effective in reducing the multiple reflections on the sections, although the very strong first multiple reflection on the April 17th section is still visible (Figure 28). Notice that the multiple reflection has an obvious reversed polarity from the primary reflection, exactly what is expected from the first primary multiple reflection. The question of the clay-layer continuity can only be answered seismically at this point by a

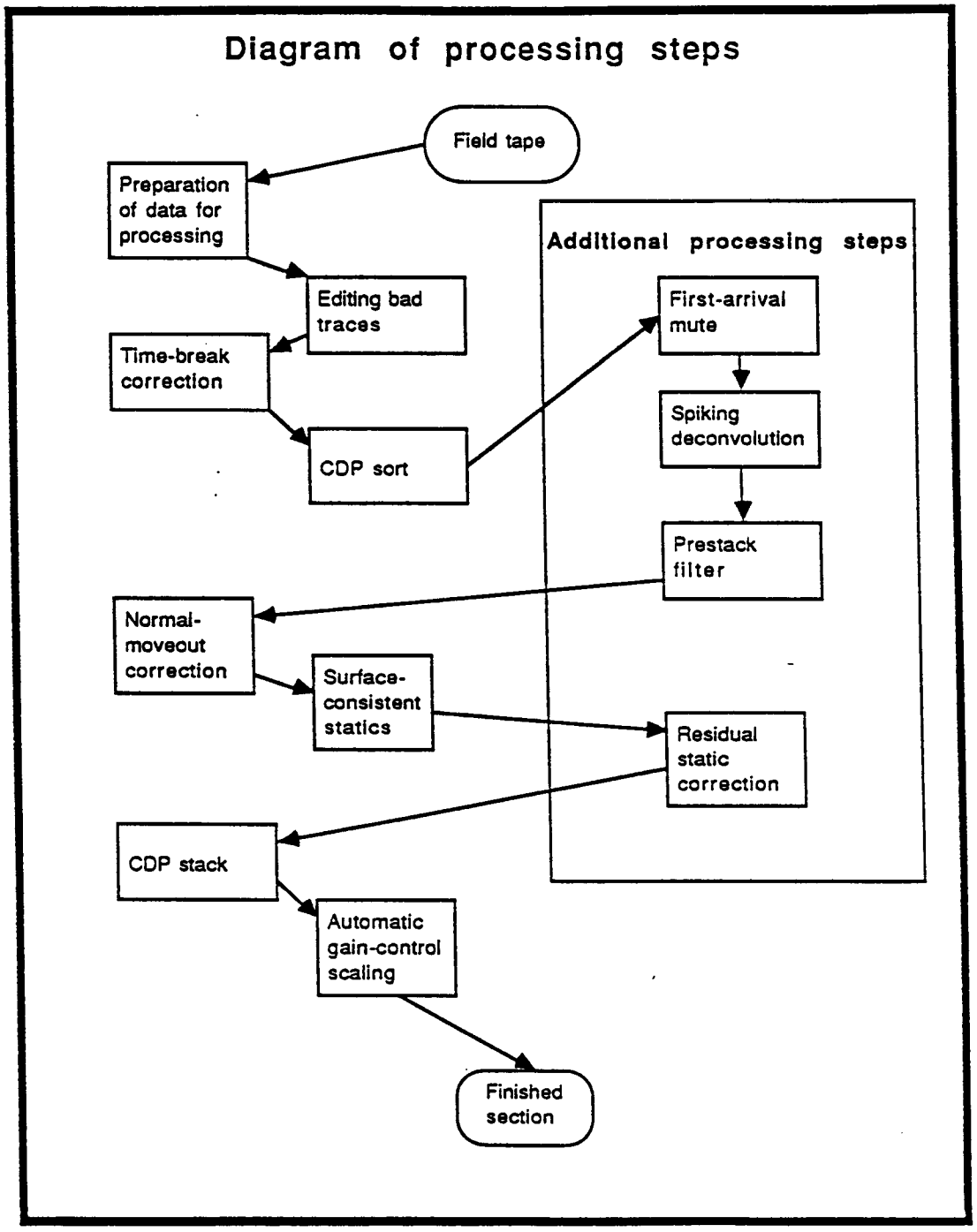

Figure 26 - Processing steps used to enhance reflection topography and any underlying clay layers.

Processing Steps	Explanation
First-arrival mute	Each trace was zeroed above the reflection to remove the air-coupled wave and the near-surface refracted wave. This allowed the next step, spiking deconvolution, to operated on data with a higher signal-to-noise ratio.
Spiking deconvolution	A filter operator was applied to the data to collapse the reflected wavelet to a spike.
Prestack filter	The data were filtered with a bandpass filter to remove unwanted high- and low-frequency noise from the data. The response cuve is shown below.
Residual static correction (residual NMO correction)	The reflected wavelets within each NMO-corrected CDP were adjusted slightly to align the wavelets before stacking. This helped prevent the reflected wavelet from dropping in frequency due to stacking wavelets not perfectly aligned.

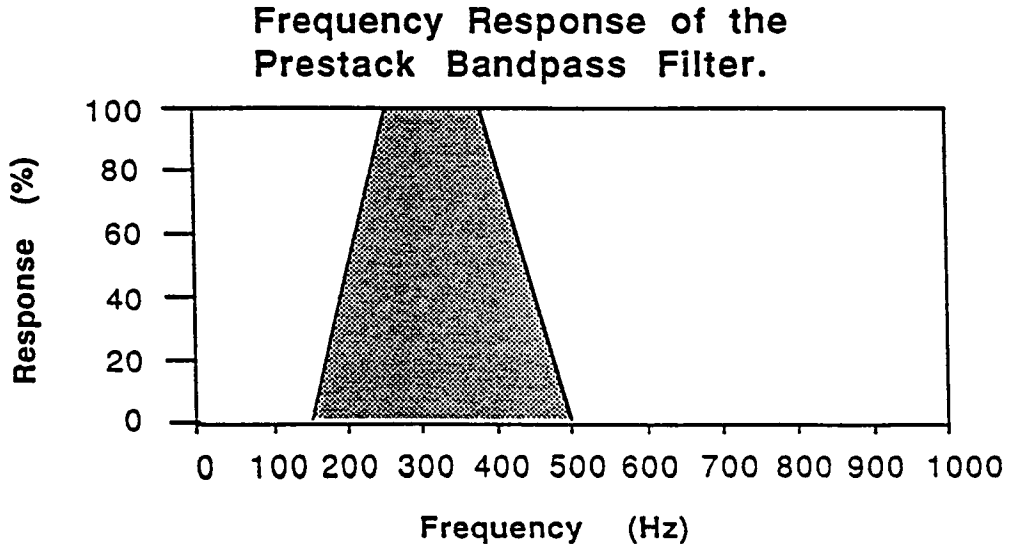

Figure 27 - Explanation of additional processing steps from Figure 26 and the frequency response of the prestack filter.

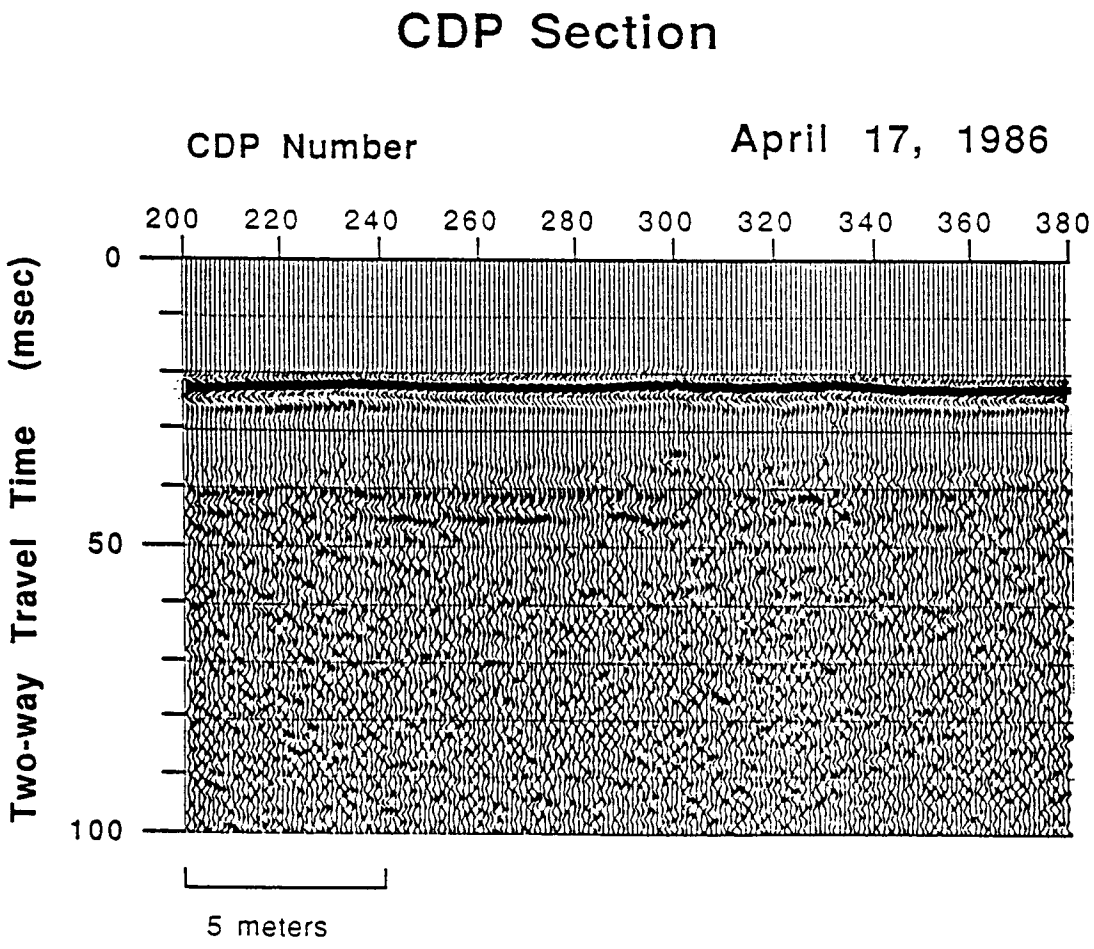

Figure 28 - CDP section recorded before pumping, processed with the same steps described in Figures 26 and 27 showing the reflection (orange) and the multiple reflection (green).

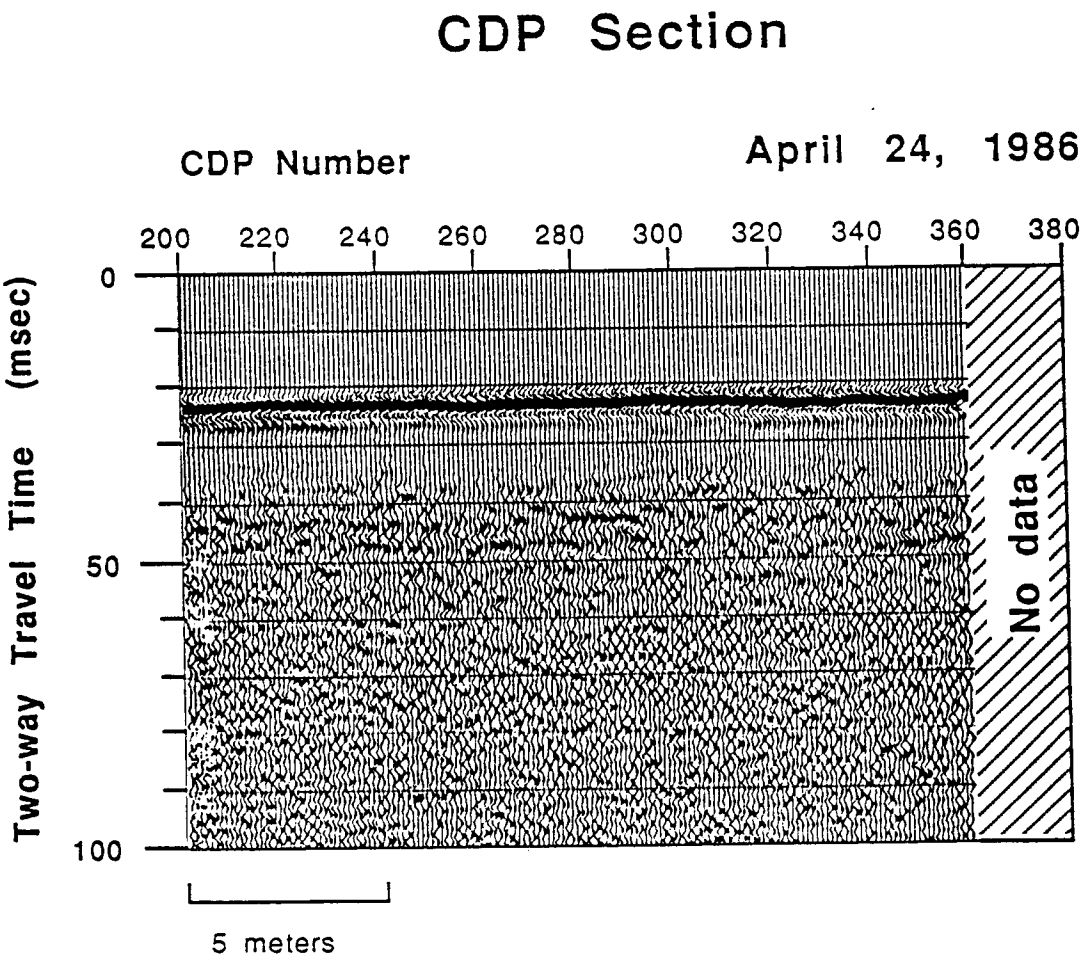

Figure 29 - CDP section recorded 3 days into the pumping test, processed with the same steps described in Figures 26 and 27 showing the reflection (orange) and the multiple reflection (green).

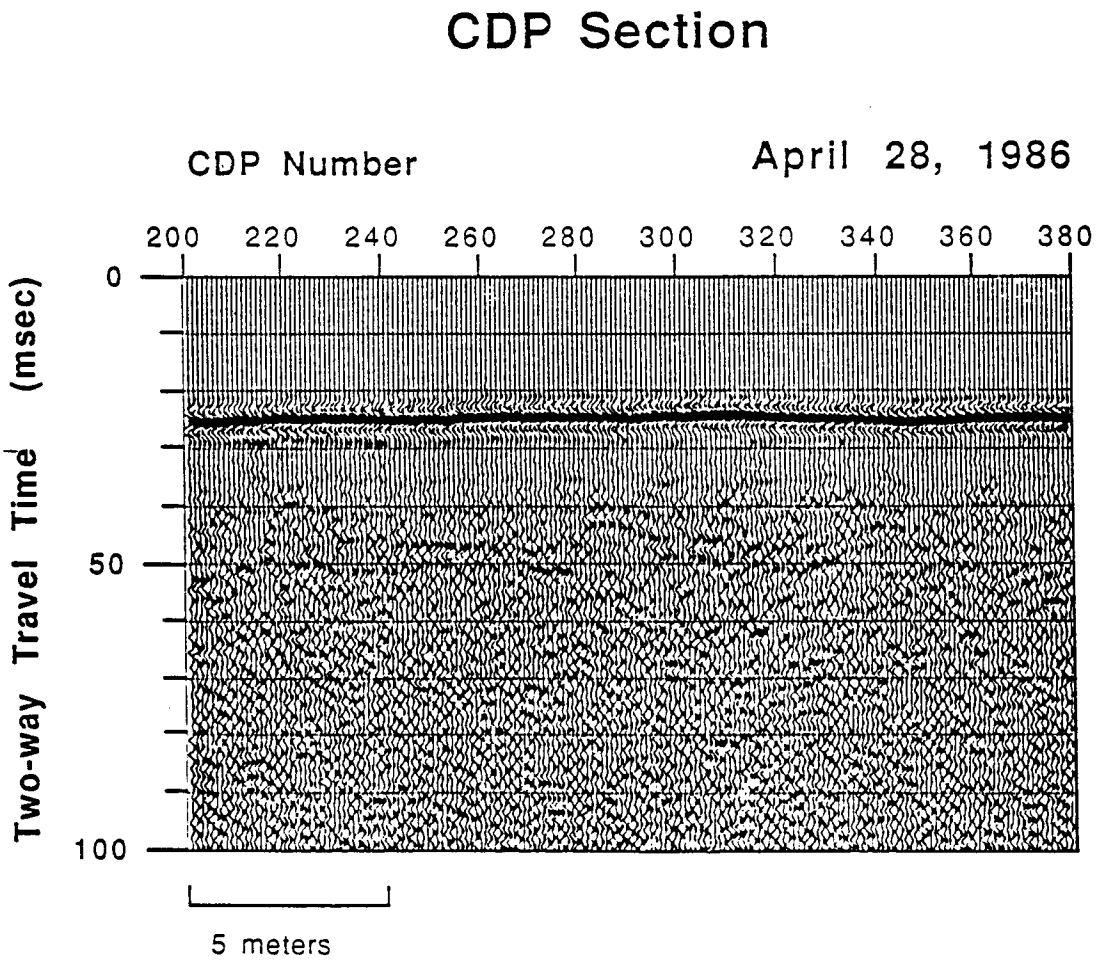

Figure 30 - CDP section recorded at maximum drawdown, processed with the same steps described in Figures 26 and 27 showing the reflection (orange) and the multiple reflection (green).

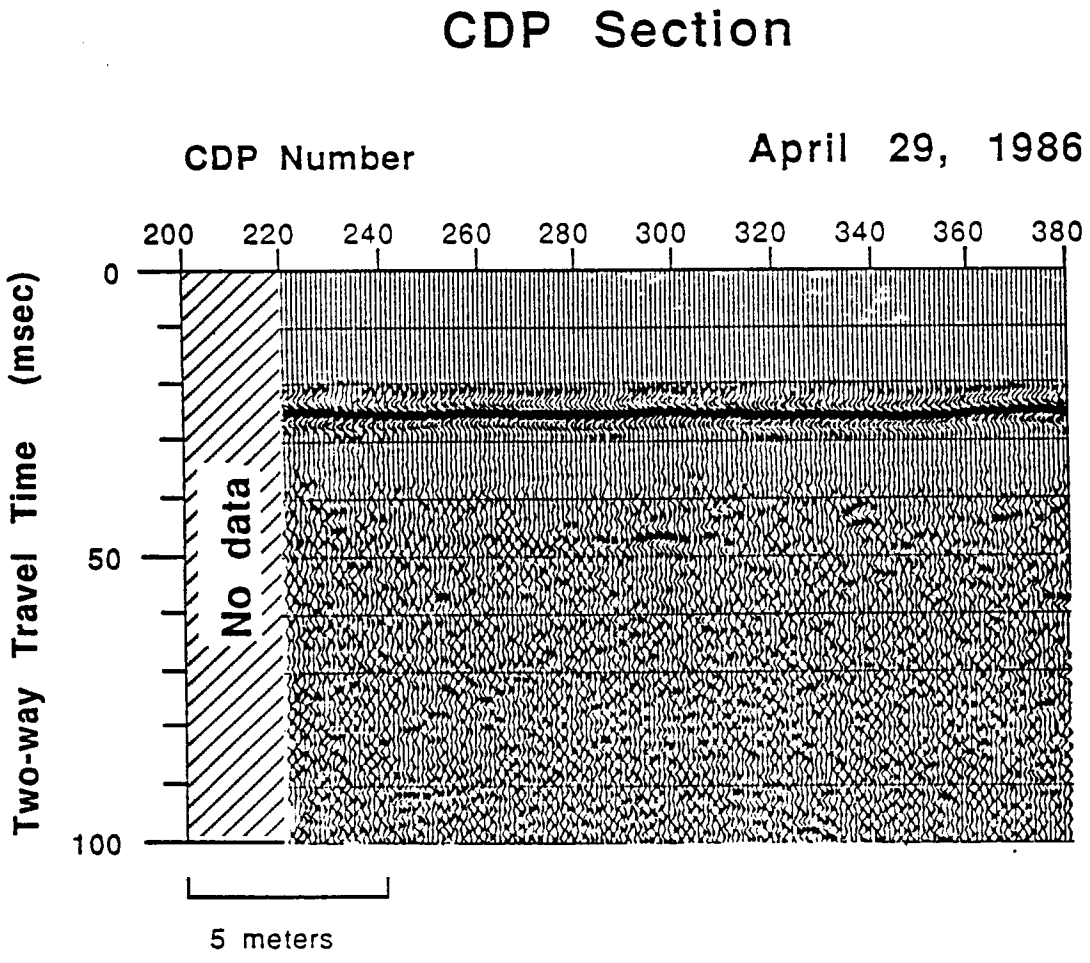

Figure 31 - CDP section recorded just after the pump was turned off, processed with the same steps described in Figures 26 and 27 showing the reflection (orange) and the multiple reflection (green).

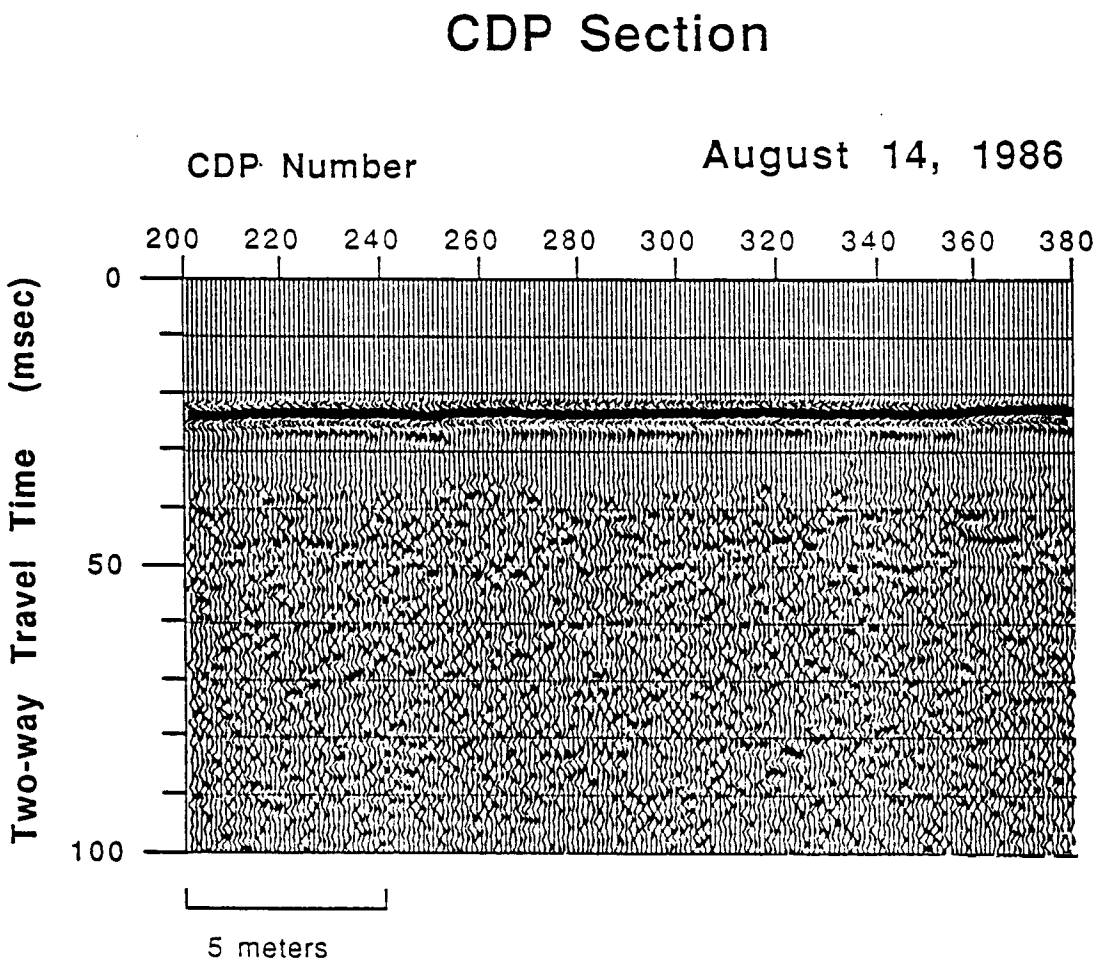

Figure 32 - CDP section recorded 4 months after the pumping test, processed with the same steps described in Figures 26 and 27 showing the reflection (orange) and the multiple reflection (green).

separate survey at the longer offsets and geophone spacings suggested by the walkaway test.

Reflection Topography

The third subject looked at in detail was the topography on the shallow reflection, especially on the April 17th CDP section (Figure 28). These humps occurred at CDPs 220-240, 296-305, and 330-338 and had a maximum relief of 0.3 m. As the pumping test continued, the humps flattened (Figures 29 to 31). Several hypotheses might explain the humps, but the most likely cause is that finer-grained sediments at those locations caused the higher elevation of the capillary fringe. It also appeared that these finer-grained sediments do not extend to the depth of the lowered saturated zone, since the humps are not observed on the later sections.

If the humps were caused by a higher capillary fringe, it might be expected that there would be some change in reflection strength along the line. In order to see if any information was contained in the relative reflection amplitudes, CDP sections were produced using the same simple processing steps as before (see Figure 17), except AGC scaling was not applied and the traces were not normalized during plotting. Figure 33 shows the portion of each section between 20 and 30 msec.

The three humps in the reflection on the April 17th section show some reduction in amplitude, reinforcing the hypothesis that the humps are showing the higher capillary-fringe elevation. If the fringe were higher and therefore thicker, the reflecting boundary

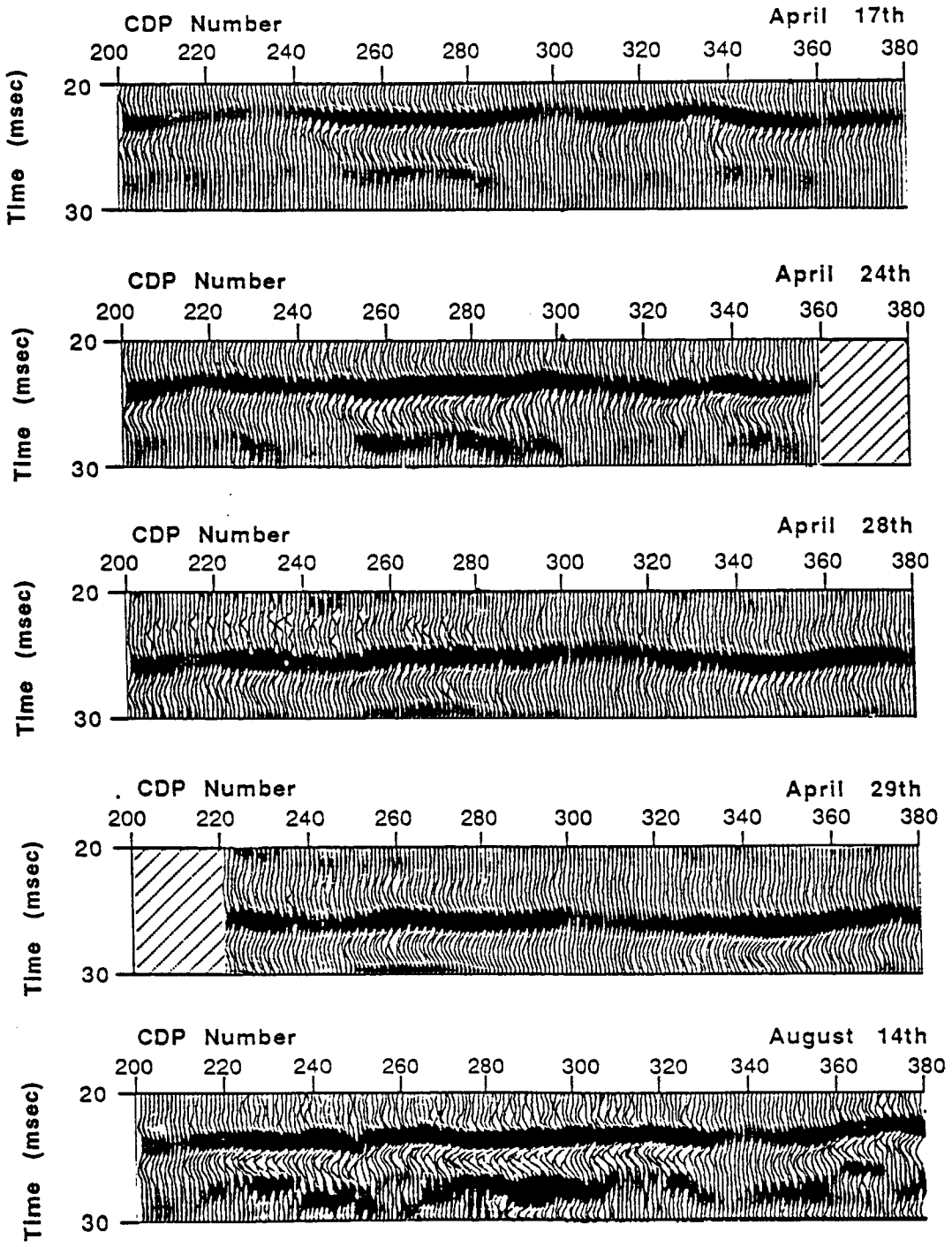

Figure 33 - True-relative-amplitude CDP sections showing the portion between 20-30 msec. The humps in the reflector, especially on the April 17th section, show amplitude reduction.

would be more diffuse, returning a signal that was weaker but higher in time on the section. The weaker signal, relative to the rest of the line, can also be seen on the individual field records (Figure 34). Also, the second peak of the near-surface refracted wave cuts across the reflection, increasing the amplitude of the reflection on traces with offsets of 3.75 m to 4.75 m where the two arrivals constructively interfere. The amplitude of the reflections then decreases on traces with offsets of 5.0 m to 6.0 m where they destructively interfere with the near-surface refracted wave. This effect is easily seen on the on the common-offset gathers (Appendix). The sections recorded after the pumping test started still show some signs of reduced amplitude in the three areas mentioned before, but the reduction is less obvious, partly because the humps are less pronounced.

The reflection between CDPs 250-290 has a higher amplitude and is flat (Figure 33). This suggests a sharper reflecting boundary, a thinner capillary fringe, and coarser sand or gravel near the top of the saturated zone. This portion of the reflection has consistently higher amplitudes throughout all five lines.

Stacking Velocities and Correlation Coefficients

Analysis of the graphs of the stacking velocities (Figure 35) and the correlation coefficients (Figure 36), calculated for the even-numbered CDP gathers using the HP-11C algorithm, helps resolve many of the subtle anomalies previously identified. The correlation coefficients are used for comparison only. The closer the number is

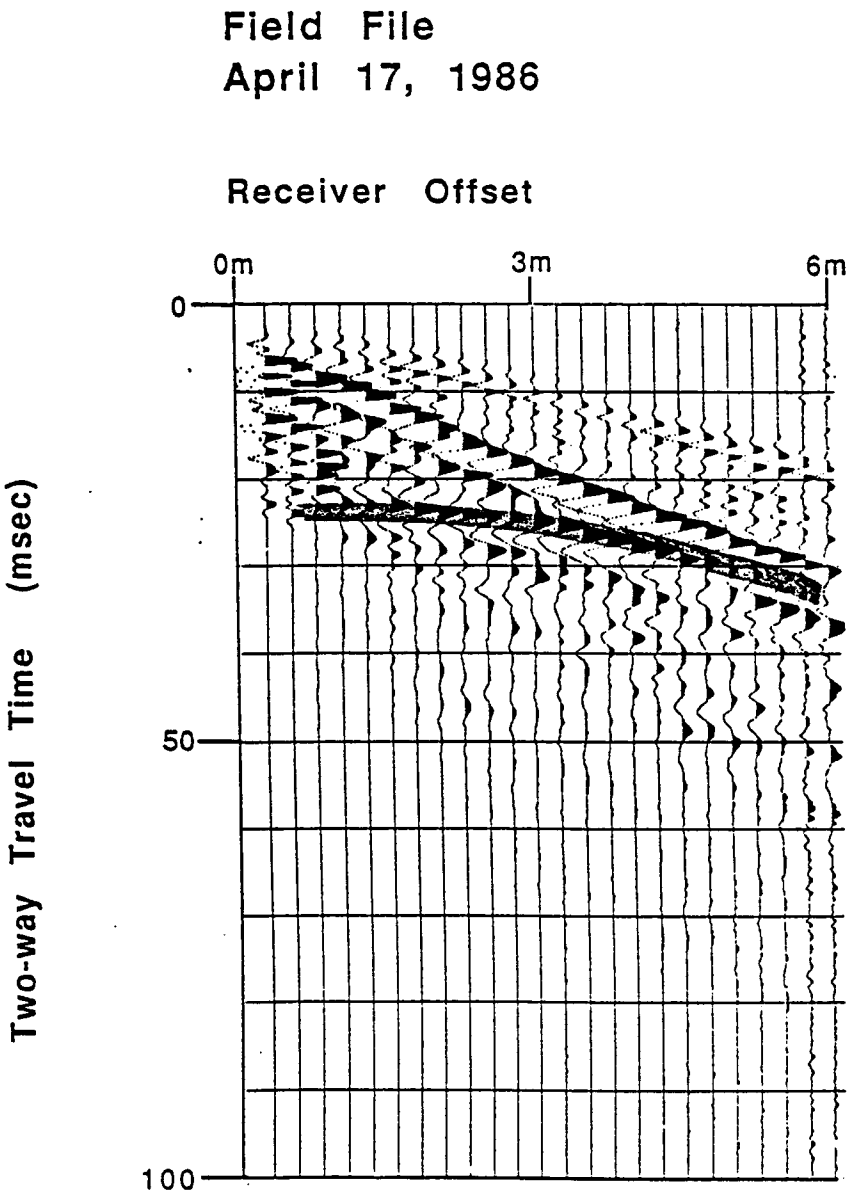

Figure 34 - Field record from a portion of the line where the reflection was weaker. Compare this reflection to the relatively strong reflection from April 17th in Figure 14.

Figure 35 - Calculated stacking velocities and the stacking-velocity function used in processing the CDP sections. The velocities calculated for the August data were higher and more uniform than for the April data.

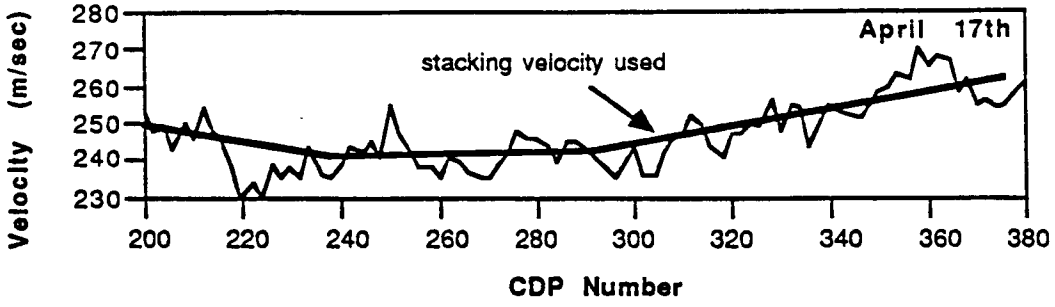
April 17th
stacking velocity used
Velocity (m/sec)
280
270
260
250
240
230
200 220 240 260 280 300 320 340 360 380
CDP Number

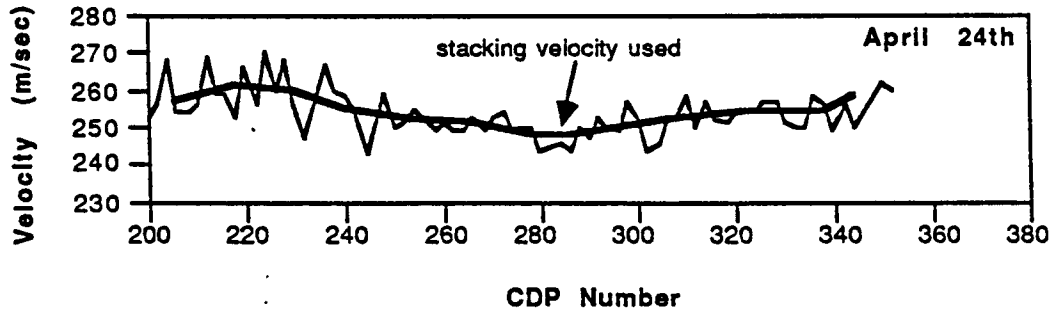
April 24th
stacking velocity used
Velocity (m/sec)
280
270
260
250
240
230
200 220 240 260 280 300 320 340 360 380
CDP Number

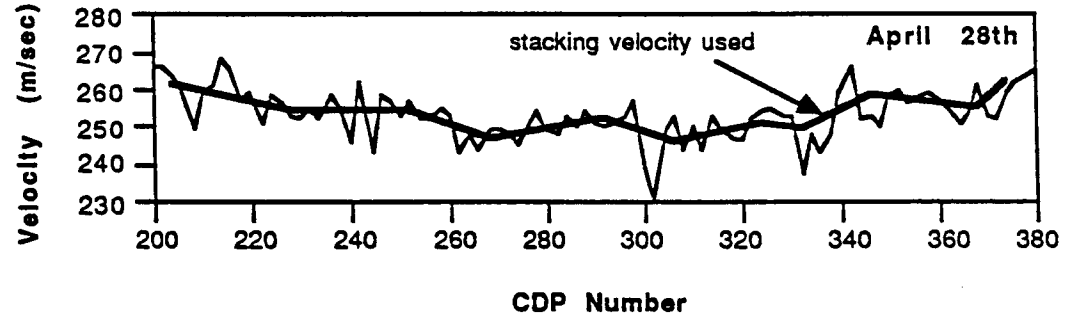
April 28th
stacking velocity used
Velocity (m/sec)
280
270
260
250
240
230
200 220 240 260 280 300 320 340 360 380
CDP Number

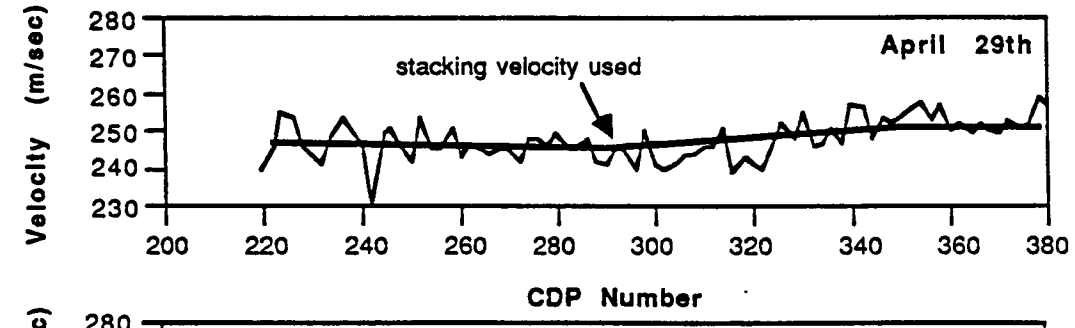
April 29th
stacking velocity used
Velocity (m/sec)
280
270
260
250
240
230
200 220 240 260 280 300 320 340 360 380
CDP Number

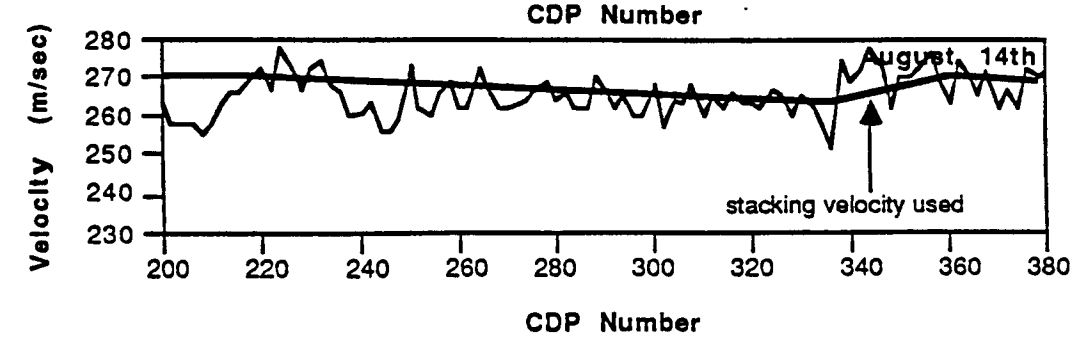
August 14th
stacking velocity used
Velocity (m/sec)
280
270
260
250
240
230
200 220 240 260 280 300 320 340 360 380
CDP Number

Figure 36 - Calculated correlation coefficients for the CDP data. Correlation coefficients of .999 to 1.000 are considered excellent for this data.

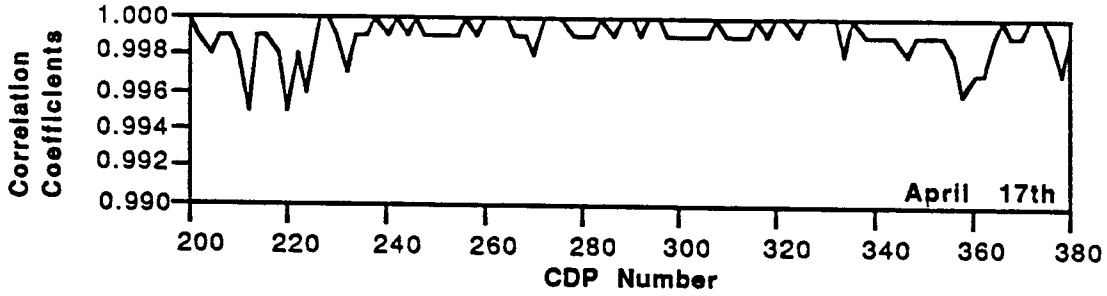
Correlation Coefficients
1.000
0.998
0.996
0.994
0.992
0.990
April 17th
200 220 240 260 280 300 320 340 360 380
CDP Number

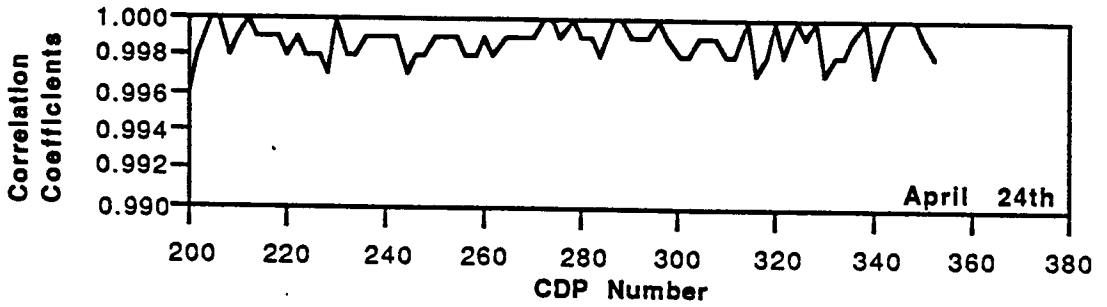
Correlation Coefficients
1.000
0.998
0.996
0.994
0.992
0.990
April 24th
200 220 240 260 280 300 320 340 360 380
CDP Number

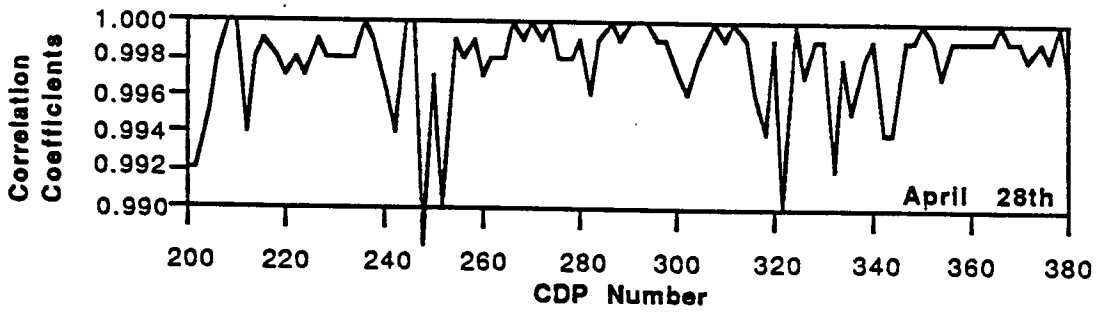
Correlation Coefficients
1.000
0.998
0.996
0.994
0.992
0.990
April 28th
200 220 240 260 280 300 320 340 360 380
CDP Number

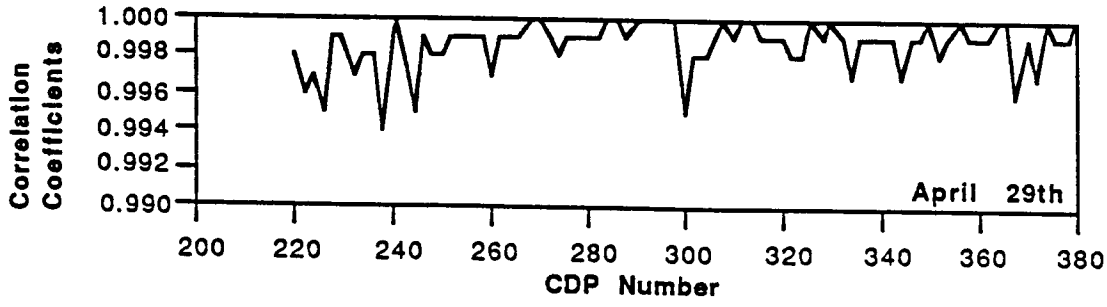
Correlation Coefficients
1.000
0.998
0.996
0.994
0.992
0.990
April 29th
200 220 240 260 280 300 320 340 360 380
CDP Number

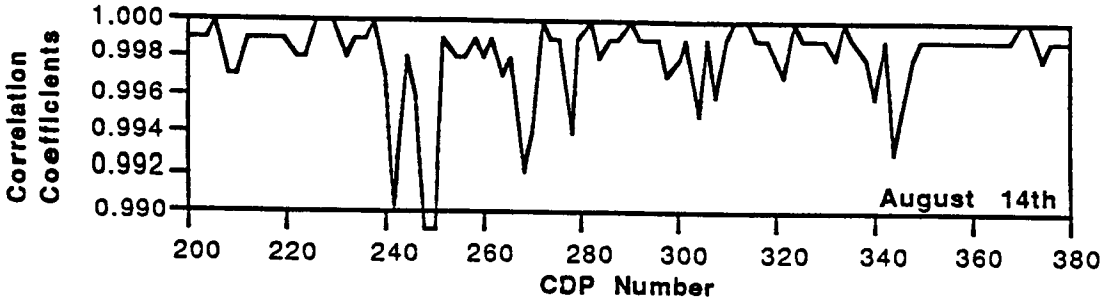
Correlation Coefficients
1.000
0.998
0.996
0.994
0.992
0.990
August 14th
200 220 240 260 280 300 320 340 360 380
CDP Number

to 1.000, the closer the measured reflection-arrival times are to the hyperbola representing the least-squares-calculated velocity. Velocities with correlation coefficients higher than 0.999 are considered excellent for this data set. A low correlation coefficient does not necessarily mean the calculated velocity and depth values are inaccurate, but less confidence can be placed in those values. The dotted line on the stacking-velocity graphs shows the NMO-stacking-velocity function used in processing the CDP sections.

The stacking-velocity graphs for the data collected in April are similar with the exception of the April 17th line. On this line, the calculated stacking velocity drops much faster across the beginning of the line than in the other three cases. The lower correlation coefficients indicate that the specific velocity values for CDPs 210-226 on the April 17th line may be incorrect, but in general, the trend is probably valid. The lower correlation coefficients in this area correspond with a drop in amplitude of the reflection and the increased interference with other coherent events noted earlier. A potential reason for the change in stacking velocities from line to line over such a short period of time could be the effects of rainstorms that occurred on April 17th after the data were collected and on April 27th.

The August 14th velocities are more uniform and are about 10-20 m/sec higher than the velocities from the April data. The moisture profile from August 14th shows a decrease in the amount of water in the 0.5-1.0 m depth range compared to the April data (Figures 21 to

23). This suggests that the extra water in the upper 1 m of the sediment creates a slow velocity layer that acts to reduce the stacking velocity for the April data. The equation for P-wave velocity is given by

$$V_p = \left[\frac{(K + 4/3\,\mu)}{q}\right]^{1/2}$$

where K is the bulk modulus (incompressibility), μ is the shear modulus, and q is the bulk density. A reduction in V_p could be caused by either an increase in density or a decrease in the quantity ($K + 4/3\,\mu$). It is difficult to say which parameters caused the change in V_p, although it probably is a combination of an increase in q and a decrease in K. If the water was being retained in the upper meter of sediment by organic-rich soil, it would not be unexpected if the amount of water retained varied laterally along the line. This might help to explain the lateral variability of the calculated stacking velocities in the April data.

The correlation coefficients tend to become less uniform and lower as the pumping test progressed. This may be attributed to several factors. As the reflecting boundary dropped and became more diffuse, the reflected signal was returned less coherently and consequently was not as good a match to a hyperbola. Another possible cause is that the source was fired into the ground close to the same spots for each line. Disturbance of the near-surface layer caused by previous shots could cause slight statics problems which might degrade the correlation coefficients. The firing of the source in close proximity to the geophones might have slightly

decoupled the geophones from the earth, resulting in a progressively worse transfer of the reflected signal to the seismograph. The rain may have also been a factor as mentioned before.

The several changing variables in these experiments prevent drawing any definite conclusions as to what caused the changes in the stacking velocities and the correlation coefficients. The amount of water in the near-surface sediments probably is a major factor though. A series of controlled experiments designed to isolate each variable would be needed to draw definite conclusions.

Conclusions

The seismic experiments at the Great Bend pumping-test site show that with proper equipment and field parameters, it is possible to obtain reflections from a hydrologic surface as shallow as 2.5 m. The strength and clarity of the reflection implies that reflections could be detected as shallow as 1-2 m under similar conditions if the need arose. It is also possible to follow the drop of this surface as the water drains out of the pore spaces in response to pumping.

This technique can be used, in conjunction with water levels from wells, to detect perched water tables. It may be possible to map the limits of a perched water table as well. The perched water table at the pumping-test site prevents drawing definite conclusions as to whether the actual reflector was the water table or the top of the saturated zone. Evidence from the neutron-probe data suggests the latter. Conclusive evidence could be found by running similar

experiments over a truly unconfined aquifer. It should be possible to map a cone of depression from a pumping well under those conditions provided enough time was allowed for the top of the saturated zone to drop down to the water table. Estimates of delayed yields might also be determined.

There is some indication that this technique may show lateral changes in lithology at the top of the saturated zone. Humps in the reflections may be an indication of a higher elevation of the capillary fringe and therefore finer sediments. It would probably be necessary to core or trench the sediments in question to find conclusive proof.

Additional work needs to be done to verify some of the other hypotheses and to determine the usefulness of this technique on other, less favorable sites. It may turn out to be possible to characterize the unsaturated portion of an unconfined aquifer by noting trends in the stacking velocities of shallow reflections. At this pumping-test site, evidence suggests that the upper 1 m of sediment, which is mainly soil, is probably responsible for most of the changes in NMO stacking velocity, both along the line and over periods time. These changes may come about because different soils retain different amounts of water for different lengths of time.

Appendix

Amplitude versus Offset

The excellent quality of data collected near Great Bend provided a unique opportunity to view the reflection amplitude as a function of offset from the source. Amplitude-versus-offset (AVO) phenomena are an energy-partitioning effect governed by P- and S-wave velocities, densities (Telford et al., 1976), and to some extent, absorption of the seismic energy. An in-depth look at the AVO effects on these data would require modeling based on the Zoeppritz equations which is beyond the scope of this study. What are presented here are some AVO observations made on the common-offset data.

These AVO data are displayed as common-offset gathers where each trace in a gather has the same source-to-receiver distance (Figure 37). The first data presented are the common-offset gathers from the four lines collected in conjunction with the pumping test (Figures 38 to 41). The traces are not normalized or scaled, although the difference in amplitude due to the seismograph gains has not been removed. Source-receiver offsets (and therefore the gather offsets of the gathers) range from 1.25 m to 6 m. The first arrival on all of the gathers is the air-coupled wave. The air-coupled wave does not line up as well across each gather on the April 24th, 28th, and 29th data sets as does the April 17th data, suggesting an increasing statics problem with time. The statics routines shift to line up the reflection at the expense of the coherency of the air-coupled wave. It may be possible to spot

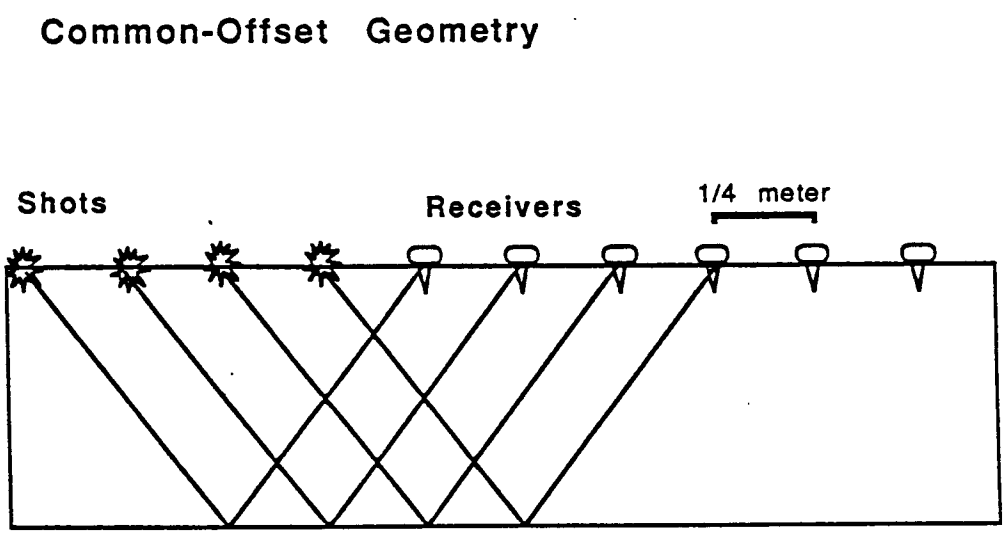

Figure 37 - Schematic diagram of a common-offset geometry. Illustrated geometry has a common offset of 1 meter.

Figure 38 - Common-offset gathers from April 17th. First number above each gather is the source-receiver offset and the second number is the angle of incidence for the reflected energy. Traces are plotted true relative amplitude within each gather although the effects of the seismograph gains have not been removed.

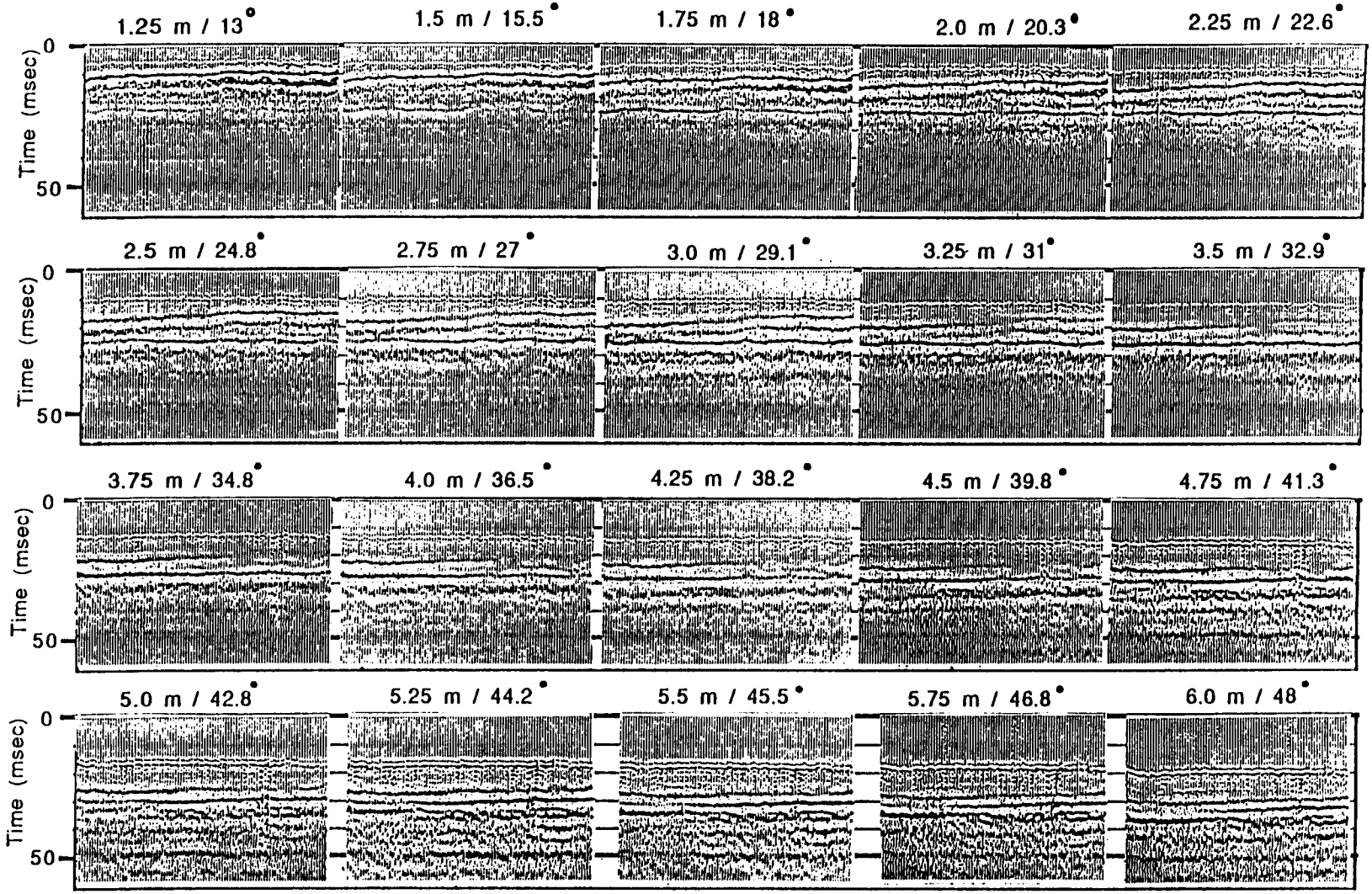
1.25 m / 13°
1.5 m / 15.5°
1.75 m / 18°
2.0 m / 20.3°
2.25 m / 22.6°
2.5 m / 24.8°
2.75 m / 27°
3.0 m / 29.1°
3.25 m / 31°
3.5 m / 32.9°
3.75 m / 34.8°
4.0 m / 36.5°
4.25 m / 38.2°
4.5 m / 39.8°
4.75 m / 41.3°
5.0 m / 42.8°
5.25 m / 44.2°
5.5 m / 45.5°
5.75 m / 46.8°
6.0 m / 48°
Time (msec)
0
50

Figure 39 - Common-offset gathers from April 24th. First number above each gather is the source-receiver offset and the second number is the angle of incidence for the reflected energy. Traces are plotted true relative amplitude within each gather although the effects of the seismograph gains have not been removed.

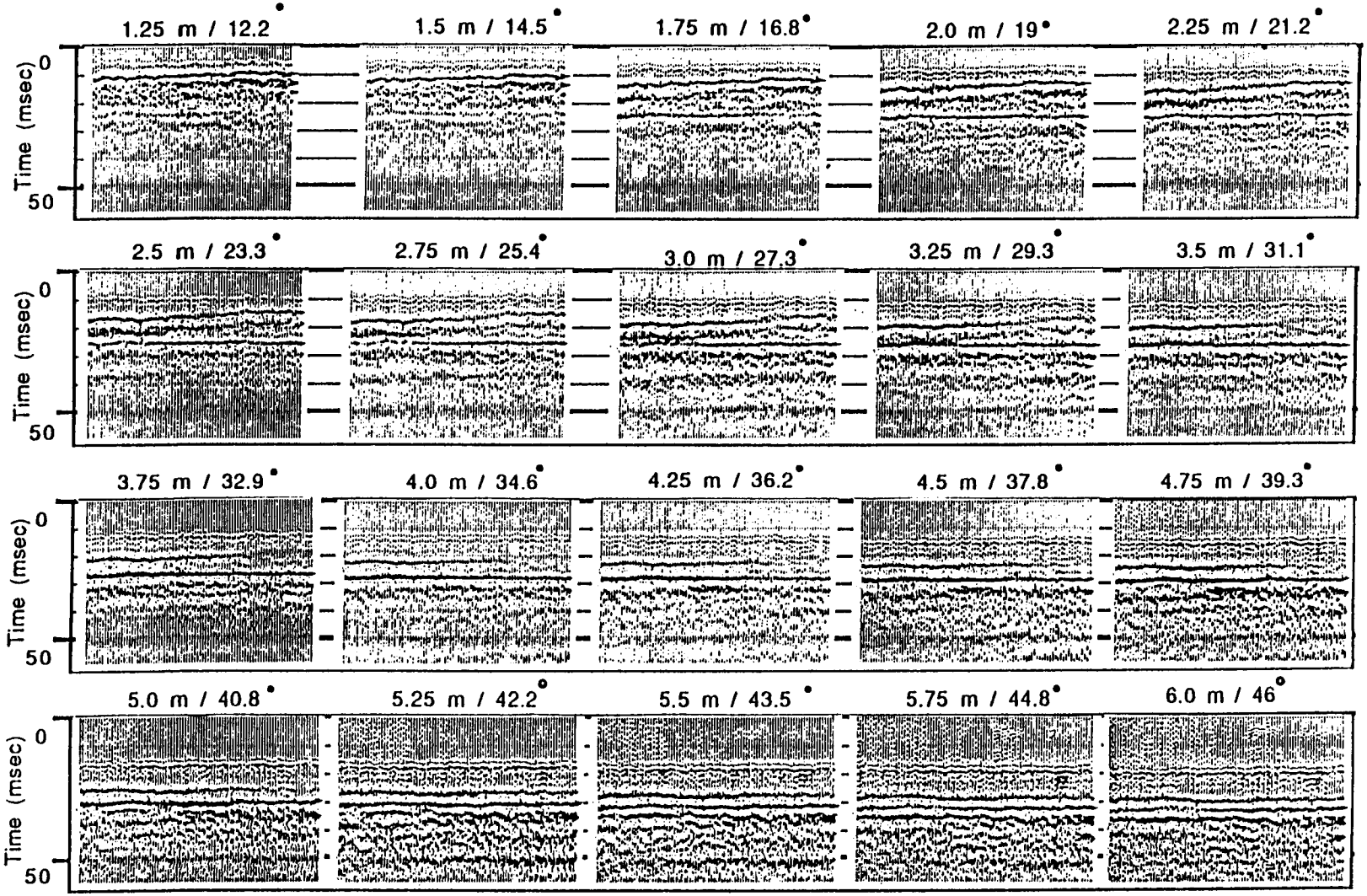
1.25 m / 12.2°
1.5 m / 14.5°
1.75 m / 16.8°
2.0 m / 19°
2.25 m / 21.2°
2.5 m / 23.3°
2.75 m / 25.4°
3.0 m / 27.3°
3.25 m / 29.3°
3.5 m / 31.1°
3.75 m / 32.9°
4.0 m / 34.6°
4.25 m / 36.2°
4.5 m / 37.8°
4.75 m / 39.3°
5.0 m / 40.8°
5.25 m / 42.2°
5.5 m / 43.5°
5.75 m / 44.8°
6.0 m / 46°
Time (msec)
0
50

Figure 40 - Common-offset gathers from April 28th. First number above each gather is the source-receiver offset and the second number is the angle of incidence for the reflected energy. Traces are plotted true relative amplitude within each gather although the effects of the seismograph gains have not been removed.

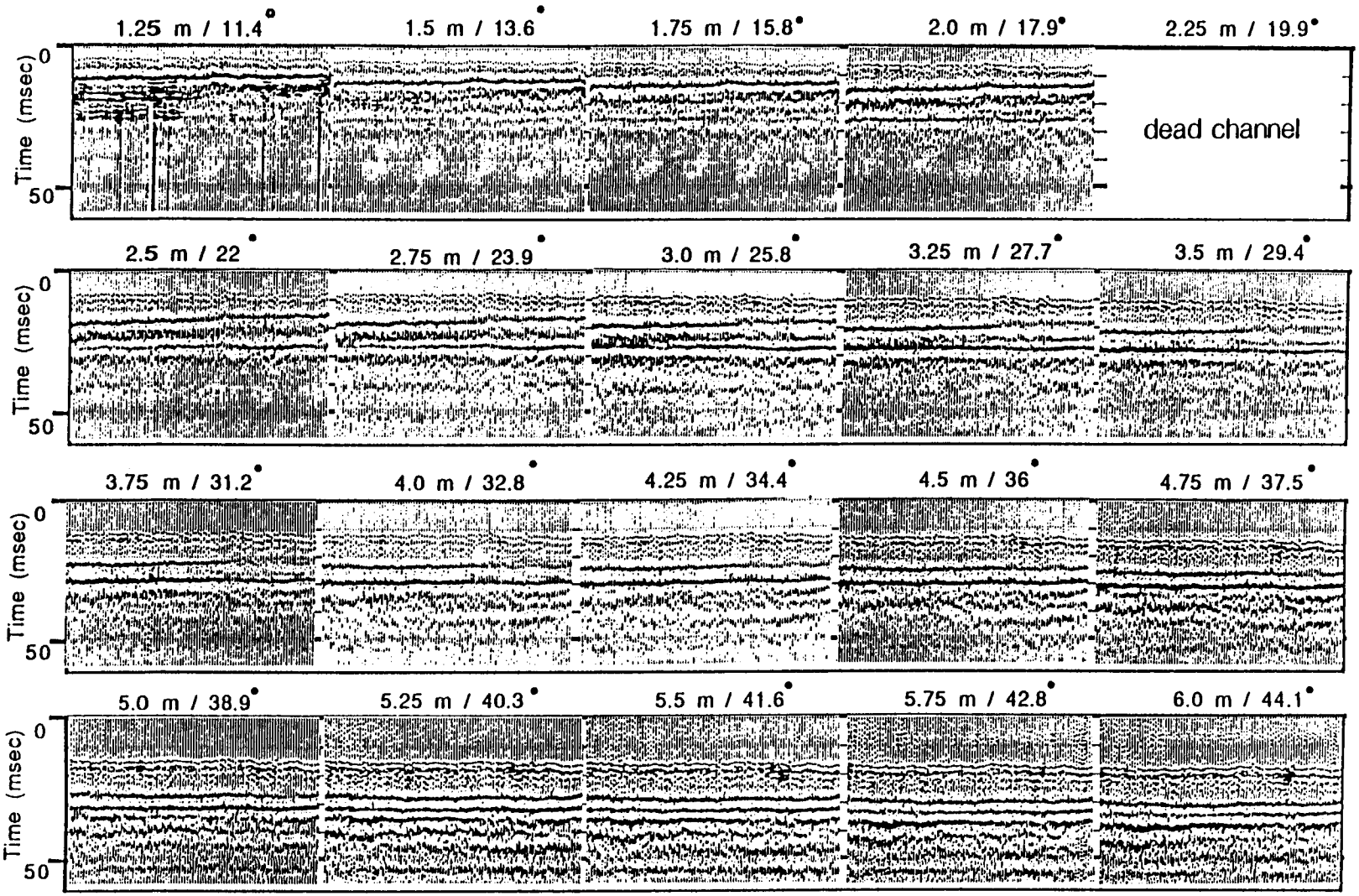
1.25 m / 11.4°
1.5 m / 13.6°
1.75 m / 15.8°
2.0 m / 17.9°
2.25 m / 19.9°
dead channel
2.5 m / 22°
2.75 m / 23.9°
3.0 m / 25.8°
3.25 m / 27.7°
3.5 m / 29.4°
3.75 m / 31.2°
4.0 m / 32.8°
4.25 m / 34.4°
4.5 m / 36°
4.75 m / 37.5°
5.0 m / 38.9°
5.25 m / 40.3°
5.5 m / 41.6°
5.75 m / 42.8°
6.0 m / 44.1°
Time (msec)
0
50

Figure 41 - Common-offset gathers from April 29th. First number above each gather is the source-receiver offset and the second number is the angle of incidence for the reflected energy. Traces are plotted true relative amplitude within each gather although the effects of the seismograph gains have not been removed.

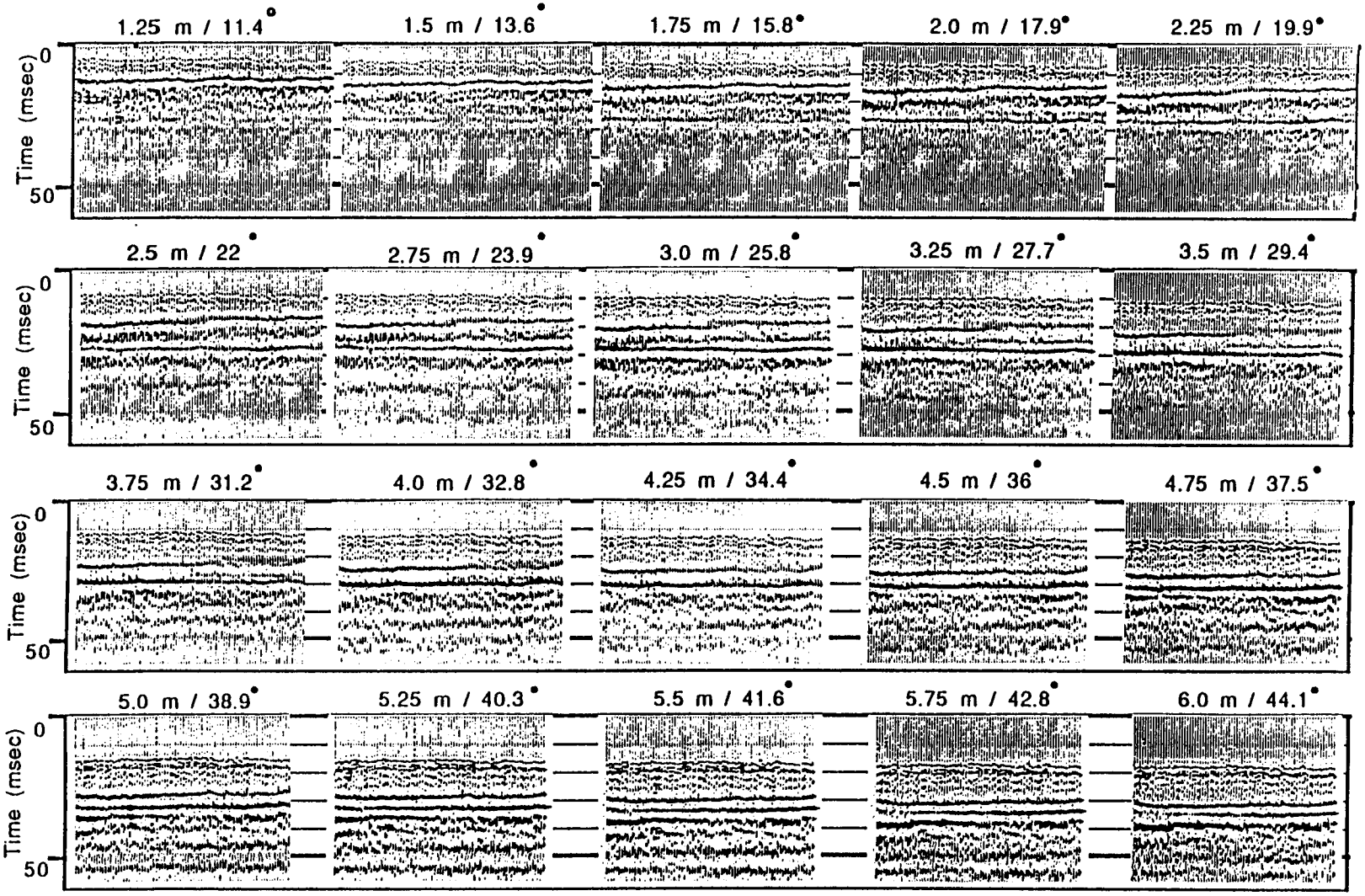
1.25 m / 11.4°
1.5 m / 13.6°
1.75 m / 15.8°
2.0 m / 17.9°
2.25 m / 19.9°
2.5 m / 22°
2.75 m / 23.9°
3.0 m / 25.8°
3.25 m / 27.7°
3.5 m / 29.4°
3.75 m / 31.2°
4.0 m / 32.8°
4.25 m / 34.4°
4.5 m / 36°
4.75 m / 37.5°
5.0 m / 38.9°
5.25 m / 40.3°
5.5 m / 41.6°
5.75 m / 42.8°
6.0 m / 44.1°
Time (msec)
0
50

spatial-aliasing problems caused by incorrect use of static correction routines by examining common-offset gathers for traces shifted by an excessive amount. This also suggests that if the velocity varies laterally along the CDP line, the best way to do time-break corrections (caused by variations in the seismograph record-start trigger) would be to align the air-coupled wave across a common-offset gather.

Direct/Refracted Wave

The second arrival is the direct/refracted wave. It is only a direct wave in the true sense on offsets of less than 1 m and beyond this the arrival has been refracted just under the soil layer about 0.5 m deep. The arrival time of the direct/refracted wave over each gather is not constant laterally. This indicates that there is a change in velocity in the horizontal direction of the near-surface sediments laterally along the line. This changing velocity tends to mimic the stacking velocity curve (Figure 35) calculated for the CDP lines, especially on the offsets around 4 m. This indicates that most of the changes in stacking velocity are due to changes in the upper 1 m of sediment. Since there is a refraction, this shows the velocity changes in the vertical direction as well as the horizontal direction.

Interference Effects

The interference phenomena between the direct/refracted arrival and the reflected arrival mentioned in the body of this thesis is

clearly illustrated on the common-offset gathers. By following the two peaks of the direct/refracted arrival as the offsets increase, it is possible to see the lower peak first merge with the reflected arrival and then drop below it. Merging of the two waves takes place at offsets around 3.25-4.5 m. This merging occurs on closer offsets on the left side of the gathers when compared to the right side. This is a function of the slower near-surface velocity on the left side of each gather.

The overall frequency of the reflection decreases on the offsets where the direct/refracted arrival and the reflected arrival constructively interfere. On the largest four offsets, especially on the April 17th data, the direct/refracted wave is low enough in time on the left side of each gather that the reflection is exactly 180 degrees out-of-phase with the direct/refracted arrival (Figure 38). This total destructive interference results in a delay in time and an increase in amplitude of the second peak of the direct/refracted arrival and a complete cancellation of the reflection.

The severity of the interference effects is dependent on the angle of incidence of the reflected energy. Common-offset gathers where the reflected energy has an angle of incidence of 44 degrees or greater show the most severe destructive interference effects.

The lack of the direct/refracted arrival on the April 17th data on offsets of 3.75 m to 5 m on the right side of the gathers is probably indicating a zone in the near surface which is absorbing a great deal of the laterally propagating energy. This zone seems to

extend from about CDP 320 to the end of the line around CDP 380. Data from the other lines show this blank portion but it is less obvious.

Multiple Reflection

The multiple reflection, visible on the April 17th common-offset data on offsets greater than 4.25 m and at about 50 msec, is also visible on the April 24th, 28th, and 29th data at the same offsets but up to 5 msec lower in time. The multiple-reflection amplitude seems to reach a maximum at an offset of 5 m on the April 17th data and at 5.25 m on the other three sets of data. The primary reflection has a fairly uniform amplitude across the different offsets which means the offsets where the multiple reflection has the greatest amplitude are also the offsets where the ratio of the multiple-reflection energy to primary-reflection energy is the highest. This may allow CDP data that have multiple-reflection problems to be edited according to offsets to remove much of the multiple-reflection energy.

The April 17th common-offset data were plotted again with the effects of the seismograph gains removed and this time, the multiple reflection has a maximum amplitude at an offset of 2.5 m and again at 5 m (Figure 42). This could correspond to the amplitude increases predicted by the Zoeppritz equations when seismic energy is incident on an acoustic-impedance boundary at the P-wave critical angle and the S-wave critical angle (Pullan and Hunter, 1985). An offset of 2.5 m for the multiple reflection means the angle of

Figure 42 - Common-offset gathers from April 17th. First number above each gather is the source-receiver offset and the second number is the angle of incidence for the reflected energy. Traces are plotted true relative amplitude with all traces plotted as if they had the same seismograph gain as the traces at 6.0-m offset. The multiple reflection has a maximum amplitude at 2.5 m and again at 5.0 m.

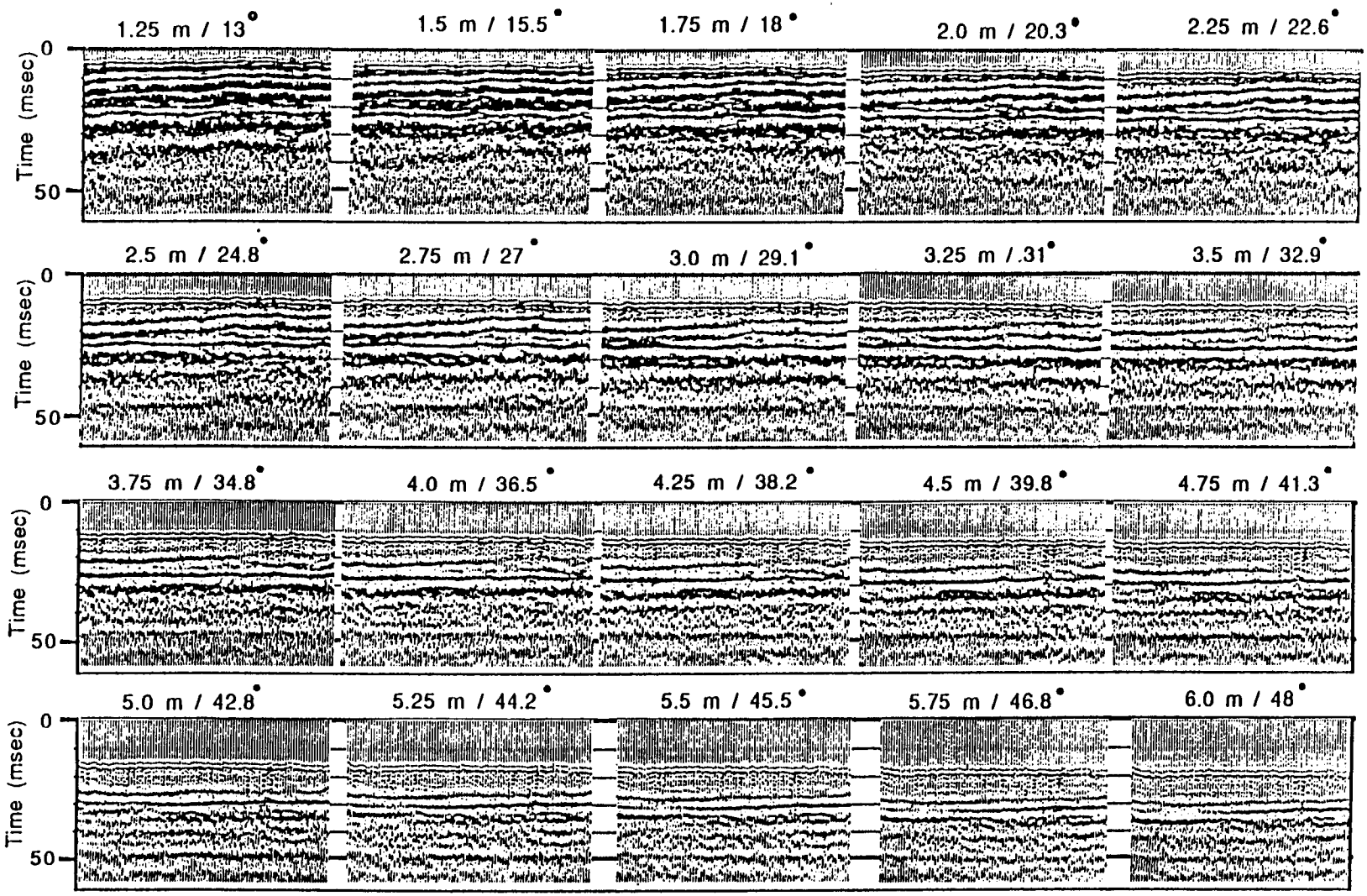
1.25 m / 13°
1.5 m / 15.5°
1.75 m / 18°
2.0 m / 20.3°
2.25 m / 22.6°
2.5 m / 24.8°
2.75 m / 27°
3.0 m / 29.1°
3.25 m / .31°
3.5 m / 32.9°
3.75 m / 34.8°
4.0 m / 36.5°
4.25 m / 38.2°
4.5 m / 39.8°
4.75 m / 41.3°
5.0 m / 42.8°
5.25 m / 44.2°
5.5 m / 45.5°
5.75 m / 46.8°
6.0 m / 48°
Time (msec)
0
50

incidence for the seismic energy was about 13 degrees, slightly larger than the value calculated for a simple two-layer model using Snell's law and refraction velocities. It is likely that the velocity distribution is more complex than a simple Snell's-law calculation can handle. There were no S-wave velocities available to check the amplitude increase that was possibly associated with the S-wave critical angle.

References

Branham, K.L., 1986, Cavity detection using high-resolution seismic reflection methods: M.S. Thesis, University of Kansas, Lawrence, Kansas, 75p.

Eaton, G.P., 1974, Seismology; in, Application of surface geophysics to ground-water investigations, A.A.R. Zohdy, G.P. Eaton, and D.R. Mabey,: U.S. Geological Survey, Techniques of water-resources investigations, Book 2- Collection of Environmental Data: 67-84.

Hunter, J.A., Pullan, S.E., Burns, R.A., Gagne, R.M., and Good, R.L., 1984, Shallow seismic reflection mapping of the overburden-bedrock interface with the engineering seismograph--some simple techniques: Geophysics, 49: 1381-1385.

Knapp, R.W., 1986, Using half-integer offset with split-spread CDP seismic data: The Leading Edge, 4: 66-69, 108.

Knapp, R.W., and Steeples, D.W., 1986a, High-resolution common-depth-point seismic profiling- Instrumentation: Geophysics, 51: 276-282.

Knapp, R.W., and Steeples, D.W., 1986b, High-resolution common-depth-point seismic profiling- Field acquisition parameter design: Geophysics, 51: 283-294.

Latta, B.F., 1950, Geology and ground-water resources of Barton and Stafford counties, Kansas: Kansas Geological Survey Bulletin 88, 228p.

Mayne, W.H., 1962, Common reflection point horizontal data stacking techniques: Geophysics, 27: 927-938.

Miller, R.D., Pullan, S.E., Waldner, J.S., and Haeni, F.P., 1986, Field comparison of shallow seismic sources: Geophysics, 51: 2067-2092.

Pullan, S.E., and Hunter, J.A., 1985, Seismic model studies of the overburden-bedrock reflection: Geophysics, 50: 1684-1688.

Schepers, R., 1975, A reflection method for solving engineering problems: J. Geophys., 41: 367-384.

Sophocleous, M.A., Townsend, M.A., Vogler, L.D., McClain, T.J., Marks, E.T., Coble, G.R., 1987, Stream-aquifer interaction along the Arkansas River in central Kansas- Field testing and analysis: Kansas Geological Survey Open-File Report 87-2, 93 p. plus Appendices.

Steeples, D.W., and Knapp, R.W., 1982, Reflections from 25 feet or less: Society of Exploration Geophysicists 52nd Annual Meeting expanded abstracts: 469-471.

Steeples, D.W., and Miller, R.D., 1986, Some shallow seismic-reflection pitfalls: Society of Exploration Geophysicists 56th Annual Meeting expanded abstracts: 101-104.

Telford, W.M., Geldart, L.P., Sheriff, R.E., and Keys, D.A., 1976, Applied Geophysics: Cambridge Press: 249-255.

Treadway, J.A., 1987, Shallow seismic study of a fault scarp near Borah Peak, Idaho: M.S. Thesis, University of Kansas, Lawrence, Kansas, 80p.